IMPROVED TRANSPORT DISCRETIZATION METHODS FOR A TWO DIMENSIONAL CYLINDRICAL GEOMETRY

A Thesis

by

CLARA BOUTROS

Submitted to the Office of Graduate and Professional Studies of
Texas A&M University
in partial fulfillment of the requirements for the degree of

MASTER OF SCIENCE

Chair of Committee,	Marvin L. Adams
Co-Chair of Committee,	Jim Morel
Committee Members,	Raytcho Lazarov
	Jean-Luc Guermond
Head of Department,	Michael Nastasi

August 2021

Major Subject: Nuclear Engineering

ABSTRACT

The purpose of this research is to provide discrete ordinates transport discretization methods for RZ geometry that have second order truncation error for the problems that have smooth solutions, accurate solution for thick diffusive problems, solution with excellent spherical symmetry for spherical problems, and that are applicable for arbitrary polygonal spatial cells. We propose spatial and angular discretization methods. We developed a Corner Balance method that uses averaged angular fluxes for each corner of a cell. We also introduced two new angle derivative treatments and applied them to the averaged Corner Balance. We tested various combinations of these methods where we used the Galerkin PWLD and CB-PWLD as references to show that the new methods improve the properties we seek.

DEDICATION

To my mother, my father, and my brother.

ACKNOWLEDGMENTS

First, I would like to thank Dr. Marvin Adams for being an excellent graduate advisor. I am grateful for his guidance and for educating me about computational methods. It has been an honor to work with him on this research. I would like to thank my committee members Dr. Jim Morel, Dr. Raytcho Lazarov and Dr. Jean-Luc Guermond. Finally, I am appreciative for Dr. Ragusa for acting as a substitute committee member during my defense, and for William Daryl Hawkins for his help to produce the plots provided in the results section.

CONTRIBUTORS AND FUNDING SOURCES

Contributors

This work was supported by a thesis committee consisting of Professor Marvin Adams, and Professor Jim Morel of the Department of Nuclear Engineering, and Professor Raytcho Lazarov and Professor Jean-Luc Guermond from the Department of Mathematics.

Funding Sources

This work was performed under the auspices of the U.S. Department of Energy by Lawrence Livermore National Laboratory under Contract DE-AC52-07NA27344.

NOMENCLATURE

CB	Corner Balance
PWLD	Piecewise Linear Discontinuous
SCB	Simple Corner Balance
MB	Multiple Balance
WD	Weighted Diamond Difference

TABLE OF CONTENTS

LIST OF FIGURES

1. INTRODUCTION

1.1 Motivation

In many applications of astrophysics and high energy density experiments, there is a need to model axisymmetric problems in cylindrical (r-z) coordinates. In a significant subset of these an important question is how far the system deviates from spherical symmetry. It is therefore important that the calculations do not introduce spherical asymmetry that is not present in the physical system being modeled. However, numerical methods for discretizing the transport equation in r-z coordinates have in the past introduced unphysical asymmetries unless they sacrifice desired properties such as conservation, accuracy, and acceptable performance in thick diffusive problems. The goal of this research is to develop spatial discretization methods that produce acceptably small deviations from spherical symmetry while rigorously conserving particles or energy, maintaining second-order accuracy in problems with smooth solutions, and providing accurate solutions in thick diffusive regions. We also require that our spatial discretization methods be applicable to spatial meshes with arbitrary polygonal cells. The latter requirement leads us to focus on "Corner-Balance" (CB) and "PieceWise Linear Discontinuous" (PWLD) finite element methods for spatial discretization. Because in r-z geometry there is a close interplay between the spatial and angular derivative terms, we also explore new treatments of the angle derivative term and investigate their impacts on accuracy and symmetry.

1.2 Transport Equation

The transport equation describes the behavior of particles as a function of particle direction, energy, and spatial location. The time dependent transport equation with anisotropic scattering is,

$$\begin{aligned}&\frac{1}{v(E)}\frac{\partial}{\partial t}\psi\left(\vec{r},E,\hat{\Omega},t\right)+\hat{\Omega}\cdot\vec{\nabla}\psi\left(\vec{r},E,\hat{\Omega},t\right)+\sigma_t\left(\vec{r},E,t\right)\psi\left(\vec{r},E,\hat{\Omega},t\right)\\&=Q\left(\vec{r},E,\hat{\Omega},t\right)+\int_0^\infty dE_i\iint_{4\pi}d\Omega_i\sigma_s\left(\vec{r},E_i\to E,\hat{\Omega}_i\to\hat{\Omega},t\right)\psi\left(\vec{r},E_i,\hat{\Omega}_i,t\right)\end{aligned}\tag{1.1}$$

where

$v(E) \equiv$ the speed of particle with kinetic energy E

$\sigma_t \equiv$ the total cross section

$\sigma_s \equiv$ the scattering cross section

$Q\left(\vec{r}, E, \hat{\Omega}, t\right) \equiv$ fixed source emission rate density of neutrons in $\vec{r}$ with kinetic energy E in direction $\hat{\Omega}$

If we apply a standard time differencing to Eq. (1.1), we get a series of steady state problems of the form,

$$\begin{aligned} &\hat{\Omega} \cdot \vec{\nabla}\psi\left(\vec{r}, E, \hat{\Omega}\right) + \sigma_t\left(\vec{r}, E\right)\psi\left(\vec{r}, E, \hat{\Omega}\right) \\ &= Q\left(\vec{r}, E, \hat{\Omega}\right) + \int_0^\infty dE_i \iint_{4\pi} d\Omega_i \sigma_s\left(\vec{r}, E_i \to E, \hat{\Omega}_i \to \hat{\Omega}\right)\psi\left(\vec{r}, E_i, \hat{\Omega}_i\right) \end{aligned} \tag{1.2}$$

If we divide the energy range into g intervals, and integrate over the gth subinterval, Eq.(1.2) becomes a multi group transport equation of the form,

$$\begin{aligned} &\hat{\Omega} \cdot \vec{\nabla}\psi_g\left(\vec{r}, \hat{\Omega}\right) + \sigma_{t,g}\left(\vec{r}\right)\psi_g\left(\vec{r}, \hat{\Omega}\right) \\ &= Q_g\left(\vec{r}, \hat{\Omega}\right) + \sum_{g'} \iint_{4\pi} d\Omega_i \sigma_{s,g' \to g}\left(\vec{r}, \hat{\Omega}_i \to \hat{\Omega}\right)\psi_{g'}\left(\vec{r}, \hat{\Omega}_i\right) \end{aligned} \tag{1.3}$$

where

$$\psi_g\left(\vec{r}, \hat{\Omega}\right) = \int_{E_g}^{E_{g-1}} dE \psi\left(\vec{r}, E, \hat{\Omega}\right) \tag{1.4}$$

$$Q_g\left(\vec{r}, \hat{\Omega}\right) = \int_{E_g}^{E_{g-1}} dE Q\left(\vec{r}, E, \hat{\Omega}\right) \tag{1.5}$$

Using an iterative method, the multi-group equation is solved by solving a series of one-group steady state transport problems of the form

$$\begin{aligned}&\hat{\Omega}\cdot\vec{\nabla}\psi\left(\vec{r},\hat{\Omega}\right)+\sigma_t\left(\vec{r}\right)\psi\left(\vec{r},\hat{\Omega}\right)\\&=Q\left(\vec{r},\hat{\Omega}\right)+\iint_{4\pi}d\Omega_i\sigma_s\left(\vec{r},\hat{\Omega}_i\rightarrow\hat{\Omega}\right)\psi\left(\vec{r},\hat{\Omega}_i\right)\end{aligned}\tag{1.6}$$

In this paper, we will use 2D cylindrical coordinates for Eq. (1.6). In conservation form [1], this becomes:

$$\begin{aligned}&\frac{\mu}{r}\frac{\partial}{\partial r}\left(r\psi(r,z,\mu,\xi)\right)+\xi\frac{\partial}{\partial z}\psi(r,z,\mu,\xi)+\frac{1}{r}\frac{\partial}{\partial\omega}\left(\eta\psi(r,z,\mu,\xi)\right)\\&+\sigma_t\psi(r,z,\mu,\xi)=Q(r,z,\mu,\xi)+\int_{-1}^{1}d\mu_i\int_{0}^{2\pi}d\xi_i\sigma_s(r,z,\mu_i,\xi_i\rightarrow\mu,\xi)\psi(r,z,\mu_i,\xi_i)\end{aligned}\tag{1.7}$$

where $\mu=\hat{\Omega}\cdot\hat{e}_r=\sin\theta\cos\omega,\xi=\hat{\Omega}\cdot\hat{e}_z=\cos\theta$, and $\eta=\sin\theta\sin\omega$. (See Fig. 2.1.)

1.3 Previous Work

In this section, we do not attempt a comprehensive review of all discretization methods that have been proposed and used for transport in cylindrical coordinates, but highlight several instances of previous work that are especially relevant to the problem we are addressing. Chaland and Samba [2] adopted an approach where they used a mixed coordinates system in which ξ as well as μ change continuously as a particle streams. This introduces a second angle-derivative term. However, this approach did not achieve many of the properties we seek in this research. For example, in this method conservation of particles is not enforced, the spatial truncation error obtained was of order 1, and given what is known about the thick diffusion limit, the method will not behave well in thick diffusive problems.

In addition, Palmer and Woods [3] employed high-order finite element methods in the solution of RZ transport equation. They applied the Galerkin DFEM and integrated the RZ transport equation over the mesh zones preserving the arbitrary-order curved mesh elements. The use of a p-order method on meshes with curved surfaces produced a $p+1$ order of truncation error for smooth solutions, but the Palmer-Woods methods do not maintain conservative properties of the transport equation.

Morel and Montry observed that the long-standing ”flux-dip” problem, in which methods did not produce zero-derivative solutions at the origin in spheres or on the axis of cylinders, could be largely eliminated by a simple change to the standard angle derivative treatment[4]. Their weighted diamond difference scheme was a step forward and is evidence that small changes in the angle-derivative treatment can have large impact on the solution near the z axis.

1.4 Specific Research Goals

Figure (1.1) shows an example polygonal symmetric grid we use in this research. The grid shown in the figure has 8 cells in the z direction(N_j) and 3 cells in the r direction(N_i). The symmetry we are seeking is basically having the same scalar flux values for the points that are the same distance from the origin. We also illustrate the h-x coordinate system in Fig. (1.2) for one cell in the spatial grid on which we seek symmetry. For each wedge, $h = 0$ at the origin of the grid and $x = 0$ at the center of the wedge. So the desired symmetry is expressed as follows: If there is no angular discretization error, then for every cell in the same ring (same distance from the origin),

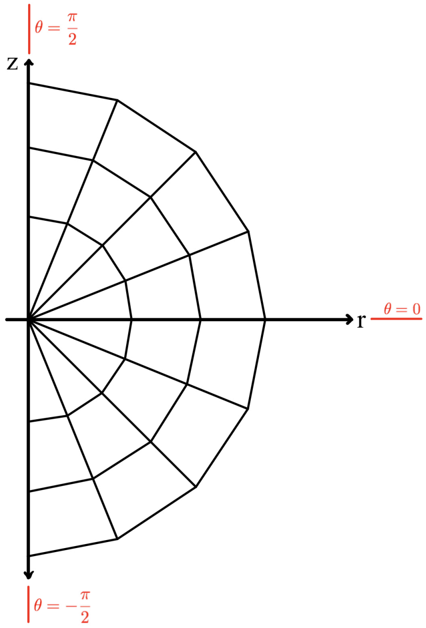

Figure 1.1: Example spatial grid with $N_i = 3$ and $N_j = 8$

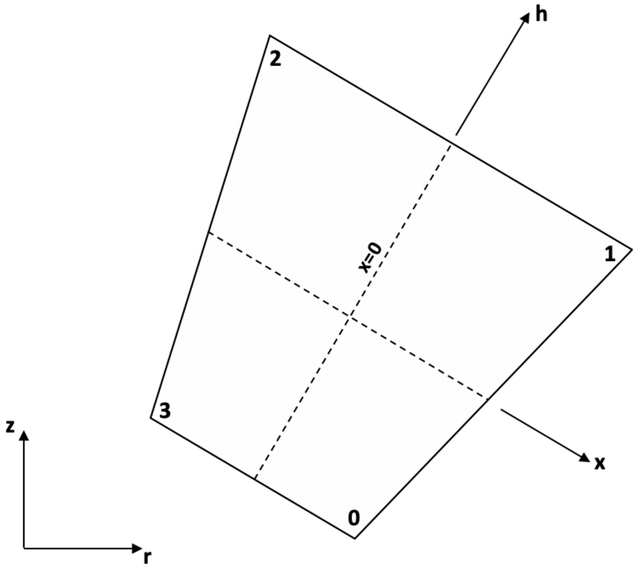

Figure 1.2: h - x coordinate system

our goal is a method for which:

$$\psi(\Omega_h, \Omega_x)_{cj} = \text{same for all cells in ring } j = 0, ..., N_j - 1 \text{ and all } c = 0, 1, 2, 3 \tag{1.8}$$

$$\psi(\Omega_h, \Omega_x)_1 = \psi(\Omega_h, -\Omega_x)_2 \tag{1.9}$$

$$\psi(\Omega_h, \Omega_x)_0 = \psi(\Omega_h, -\Omega_x)_3 \tag{1.10}$$

The Galerkin PWLD method has three of the desired characteristics; second order truncation error, applicability to polygonal cells, and accurate solutions in thick diffusion limit[7]. However, this method produces more spherical asymmetry than is desired, so our goal is to develop a new method that improves the symmetry for the spherical problems while maintaining the properties achieved by the Galerkin PWLD.

1.5 Overview of Chapters

In Chapter 2, we describe a family of DFEMs with standard angle derivative treatment and show the general form of the equation on which the methods considered here will be based. We demonstrate lumping techniques in RZ geometry and note their role in improving monotonicity of solutions.

In Chapter 3, we define the PWLD method (a particular DFEM) and explicitly define the associated matrices. We start with the Galerkin method that uses weight functions equal to the PWL basis functions. We then implement the Corner Balance PWLD, a Petrov-Galerkin method that integrates the transport equation over each corner subcell volume. And finally, we introduce a generalized Corner Balance PWLD method and show that one member of this family is the ”Simple Corner Balance” (SCB) method[8].

In Chapter 4, we explore an alternative angular discretization technique. The standard technique involves collocation at quadrature points, whereas the alternatives integrate the equations over the angle bins. The main new alternative we consider, “Multiple Balance”, integrates the equations over both full-range and half-range angle bins.

In Chapter 5, we show the behavior of several spatial discretizations using the standard angle discretization and the SCB spatial method with several different angle discretization methods. Our main test problem employs a manufactured solution with spherical symmetry, and we study solution behavior as a function of the numbers of polar quadrature points, azimuthal quadrature points, rings in the spatial grid and wedges in the spatial grid. We analyze the graphs and explain the issues we encountered.

In the final chapter, we conclude with a brief summary of the research and offer some suggestions future work that might generate further improvements in RZ transport discretization methods.

2. DISCONTINUOUS FINITE ELEMENT METHODS IN RZ GEOMETRY

2.1 Overview of Discontinuous Finite Elements Methods with Standard Angle Derivative Treatment

The r-z transport equation is of the form[1],

$$\frac{\mu}{r}\frac{\partial}{\partial r}(r\psi)+\xi\frac{\partial}{\partial z}\psi+\frac{1}{r}\frac{\partial}{\partial \omega}(\eta\psi)+\sigma_t\psi(r,z,\mu,\xi)=q(r,z,\mu,\xi), \tag{2.1}$$

where q is the total source rate density. Assuming isotropic scattering and an isotropic source, $q(r,z,\mu,\xi)$ becomes independent of all angles and defined as follows,

$$q(r,z)=\frac{1}{2\pi}\left(\sigma_s\phi(r,z)+Q(r,z)\right). \tag{2.2}$$

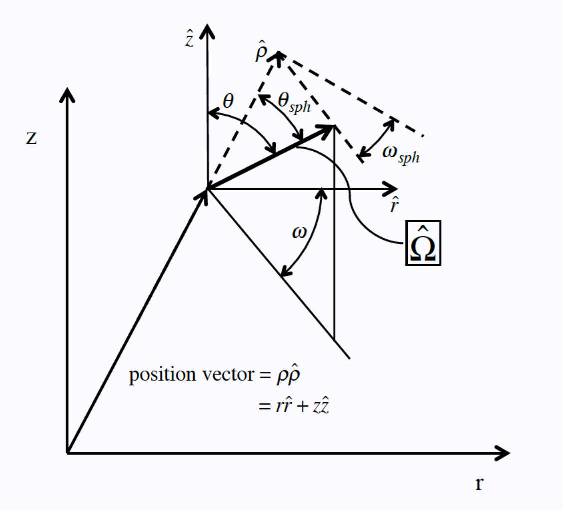

Figure 2.1: Angles θ and ω on $r-z$ plane

The direction variables are defined as functions of angles θ and ω from Fig (2.1),

$$\xi=\cos(\theta) \tag{2.3}$$

$$\mu = \sin(\theta)\cos(\omega) \tag{2.4}$$

$$\eta = \sin(\theta)\sin(\omega) \tag{2.5}$$

For this method, N_p polar levels of ξ are used, with the p^{th} level containing $N_{p,q}$ azimuthal angles $\mu_{p,q}$. The weights $w_{p,q}$ sum to 2π. The discrete form of the transport equation is written as follows[1]

$$\begin{gathered}\frac{\mu_{p,q}}{r}\frac{\partial}{\partial r}(r\psi_{p,q}) + \xi_p\frac{\partial}{\partial z}\psi_{p,q} + \frac{\alpha_{p,q+1/2}\psi_{p,q+1/2} - \alpha_{p,q-1/2}\psi_{p,q-1/2}}{rw_{p,q}} \\ +\sigma_t\psi_{p,q}(r,z) = q(r,z),\end{gathered} \tag{2.6}$$

where we discretize the angular derivative term using differencing coefficients that preserve the constant solution in space and time. The differencing coefficients are defined as follows

$$\alpha_{p,q+1/2} = \alpha_{p,q-1/2} - w_{p,q}\mu_{p,q} \tag{2.7}$$

$$\alpha_{1/2} = \alpha_{N_q+1/2} = 0 \tag{2.8}$$

We then use Morel and Montry's [4] weighted diamond difference scheme that is exact for a linear in angle solution,

$$\psi_{p,q}(r,z) = \tau_{p,q}\psi_{p,q+1/2}(r,z) + (1-\tau_{p,q})\psi_{p,q-1/2}(r,z) \tag{2.9}$$

where

$$\tau_{p,q} = \frac{\mu_{p,q} - \mu_{p,q-1/2}}{\mu_{p,q+1/2} - \mu_{p,q-1/2}} \tag{2.10}$$

We now rewrite Eq. (2.6) after using Eq. (2.9) to eliminate $\psi_{p,q+1/2}$

$$\begin{gathered}\frac{\mu_{p,q}}{r}\frac{\partial}{\partial r}(r\psi_{p,q}) + \xi_p\frac{\partial}{\partial z}\psi_{p,q} + \frac{\frac{\alpha_{p,q+1/2}}{\tau_{p,q}}\psi_{p,q} - \left(\frac{1-\tau_{p,q}}{\tau_{p,q}}\alpha_{p,q+1/2} + \alpha_{p,q-1/2}\right)\psi_{p,q-1/2}}{rw_{p,q}} \\ + \sigma_t\psi_{p,q}(r,z) = q(r,z),\end{gathered} \tag{2.11}$$

After rearranging, the left hand side contains the unknown $\psi_{p,q}$,

$$\begin{aligned} &\frac{\mu_{p,q}}{r}\frac{\partial}{\partial r}(r\psi_{p,q}) + \xi_p\frac{\partial}{\partial z}\psi_{p,q} + \frac{1}{rw_{p,q}}\frac{\alpha_{p,q+1/2}}{\tau_{p,q}}\psi_{p,q} + \sigma_t\psi_{p,q}(r,z) \\ &= q(r,z) + \frac{1}{rw_{p,q}}\left(\frac{1-\tau_{p,q}}{\tau_{p,q}}\alpha_{p,q+1/2} + \alpha_{p,q-1/2}\right)\psi_{p,q-1/2}, \end{aligned} \tag{2.12}$$

Equations (2.12) and (2.9) given $\psi_{p,q}$ and $\psi_{p,q+1/2}$ in terms of $\psi_{p,q-1/2}$. The solution is obtained by marching through the angle bins in order of increasing q. When $q = 1$, a value is needed for $\psi_{p,1/2}$, which is associated with $\omega = \pi$ and is called the "starting direction." The right hand side now contains $\psi_{p,q-1/2}$ which implies that this value is known from the sweeping order resulting from solving for the angular flux associated with $\omega = \pi$. This direction is called the starting direction and it is solved with the following equation,

$$\mu_{p,1/2}\frac{\partial}{\partial r}\psi_{p,1/2} + \xi_p\frac{\partial}{\partial z}\psi_{p,1/2} + \sigma_t\psi_{p,1/2}(r,z) = q(r,z) \tag{2.13}$$

where μ of the starting direction is defined as

$$\mu_{p,1/2} = -\left(1-\xi_p^2\right)^{\frac{1}{2}} \tag{2.14}$$

With the standard discrete-ordinates equations now defined, we derive the equations that define general family of DFEM methods. We follow the treatment given by Adams [5]. We begin with multiplying Eq (2.12) by r and by the weight function v_i and integrating over the cell volume,

$$\begin{aligned} &\iint drdz\, v_i\left[\mu_{p,q}\frac{\partial}{\partial r}(r\psi_{p,q}) + r\xi_p\frac{\partial}{\partial z}\psi_{p,q} + \frac{1}{w_{p,q}}\frac{\alpha_{p,q+1/2}}{\tau_{p,q}}\psi_{p,q} + r\sigma_t\psi_{p,q}(r,z)\right] \\ &= \iint drdz\, v_i\left[rq(r,z) + \frac{1}{w_{p,q}}\left(\frac{1-\tau_{p,q}}{\tau_{p,q}}\alpha_{p,q+1/2} + \alpha_{p,q-1/2}\right)\psi_{p,q-1/2}\right], \end{aligned} \tag{2.15}$$

Writing the first two terms as a dot product,

$$\begin{aligned}&\iint drdz\, v_i \left[\hat{\Omega}\cdot\vec{\nabla}\psi_{p,q} + \frac{1}{w_{p,q}}\frac{\alpha_{p,q+1/2}}{\tau_{p,q}}\psi_{p,q} + r\sigma_t\psi_{p,q}(r,z)\right] \\ &= \iint drdz\, v_i \left[rq(r,z) + \frac{1}{w_{p,q}}\left(\frac{1-\tau_{p,q}}{\tau_{p,q}}\alpha_{p,q+1/2} + \alpha_{p,q-1/2}\right)\psi_{p,q-1/2}\right],\end{aligned} \tag{2.16}$$

Applying Gauss Divergence theorem on the spatial derivative term,

$$\begin{aligned}&\oint_{\partial A} d\ell v_i \hat{e}_n\cdot\hat{\Omega}(r\tilde{\psi}_{p,q}) - \iint drdz(r\psi_{p,q})\hat{\Omega}\cdot\vec{\nabla}v_i + \iint drdz\, v_i\left[\frac{1}{w_{p,q}}\frac{\alpha_{p,q+1/2}}{\tau_{p,q}}\psi_{p,q} + r\sigma_t\psi_{p,q}(r,z)\right] \\ &= \iint drdz\, v_i \left[rq(r,z) + \frac{1}{w_{p,q}}\left(\frac{1-\tau_{p,q}}{\tau_{p,q}}\alpha_{p,q+1/2} + \alpha_{p,q-1/2}\right)\psi_{p,q-1/2}\right],\end{aligned} \tag{2.17}$$

The $\tilde{\psi}$ represents the angular flux on the surface of the cell. These values are determined based on the "upstream" flux values as follows

$$\tilde{\psi}_{p,q} = \begin{cases} \psi_{p,q,cell} & \text{if} \quad \hat{e}_n\cdot\hat{\Omega} > 0 \\ \psi_{p,q,upstream\,cell} \text{ or } \psi_{p,q,boundary} & \text{if} \quad \hat{e}_n\cdot\hat{\Omega} < 0 \end{cases} \tag{2.18}$$

and the angular flux can be approximated as a combination of basis functions

$$\psi_{p,q} = \sum_{c=1}^{C}\psi_{p,q,c}(r,z)b_c(r,z) \tag{2.19}$$

where c denotes the cell vertex associated with corner subcell c. Equation (2.17) becomes,

$$\begin{aligned}&\oint_{\partial A} d\ell v_i\hat{e}_n\cdot\hat{\Omega}r\sum_{c=1}^{C}\tilde{\psi}_{p,q,c}b_c(r,z) - \iint drdz\left(r\sum_{c=1}^{C}\psi_{p,q,c}b_c(r,z)\right)\hat{\Omega}\cdot\vec{\nabla}v_i \\ &+ \iint drdz\, v_i\left[\frac{1}{w_{p,q}}\frac{\alpha_{p,q+1/2}}{\tau_{p,q}}\sum_{c=1}^{C}\psi_{p,q,c}b_c(r,z) + r\sigma_t\sum_{c=1}^{C}\psi_{p,q,c}b_c(r,z)\right] \\ &= \iint drdz\, v_i\left[r\sum_{c=1}^{C}q_c(r,z)b_c(r,z) + \frac{1}{w_{p,q}}\left(\frac{1-\tau_{p,q}}{\tau_{p,q}}\alpha_{p,q+1/2} + \alpha_{p,q-1/2}\right)\sum_{c=1}^{C}\psi_{p,q-1/2,c}b_c(r,z)\right],\end{aligned} \tag{2.20}$$

The corresponding starting direction equation is of the form,

$$\begin{aligned}\oint_{\partial A} d\ell r v_i \hat{e}_n \cdot \hat{\Omega} \sum_{c=1}^{C} \tilde{\psi}_{p,1/2,c} b_c(r,z) - \iint drdzr \left(\sum_{c=1}^{C} \psi_{p,1/2,c} b_c(r,z) \right) \hat{\Omega} \cdot \vec{\nabla} v_i \\ + \iint drdz\, v_i r \left[-\mu_{p,1/2} \sum_{c=1}^{C} \psi_{p,1/2,c} b_c(r,z) + \sigma_t \sum_{c=1}^{C} \psi_{p,1/2,c} b_c(r,z) \right] \\ = \iint drdz\, v_i r \sum_{c=1}^{C} q_c(r,z) b_c(r,z),\end{aligned} \tag{2.21}$$

2.2 Lumping in RZ Geometry

Lumping reduces the tendency of discretization methods to overshoot and undershoot the true maxima and minima of the solution[5]. The fully lumped method is localizing the collision term, the source term, and the surface integral terms in the interior vertex of the cell. Starting with the transport equation

$$\frac{\mu}{r}\frac{\partial}{\partial r}(r\psi) + \xi \frac{\partial}{\partial z}\psi + \frac{1}{r}\frac{\partial}{\partial \omega}(\eta\psi) + \sigma_t \psi = q, \tag{2.22}$$

Multiplying by the weight function v_i, then integrating over cell volume

$$\iint drdzrv_i \left[\frac{\mu}{r}\frac{\partial}{\partial r}(r\psi) + \xi \frac{\partial}{\partial z}\psi - \frac{1}{r}\frac{\partial}{\partial \omega}(\eta\psi) + \sigma_t \psi \right] = \iint drdzrv_i q, \tag{2.23}$$

Applying the Gauss Divergence theorem to the spatial derivative term

$$\begin{aligned}\oiint drdzrv_i \hat{e}_n \cdot \hat{\Omega} \tilde{\psi} - \iint drdzr\psi \hat{\Omega} \cdot \vec{\nabla} v_i - \iint drdzv_i \frac{\partial}{\partial \omega}(\eta\psi) \\ + \iint drdzrv_i \sigma_t \psi = \iint drdzrv_i q\end{aligned} \tag{2.24}$$

The fully lumped version of Eq (2.24) is,

$$\begin{aligned}\tilde{\psi}_i \oiint drdzrv_i \hat{e}_n \cdot \hat{\Omega} - \psi_i \iint drdzr \hat{\Omega} \cdot \vec{\nabla} v_i - \psi_i \iint drdzv_i \frac{\partial \eta}{\partial \omega} \\ + \psi_i \iint drdzrv_i \sigma_t = q_i \iint drdzrv_i\end{aligned} \tag{2.25}$$

2.3 Summary

In this chapter, we outlined a derivation of a family of Discontinuous Finite Element Methods (DFEMs) for RZ problems. Starting with r-z transport equation, we defined our grid and directional variables. We applied discrete values of polar and azimuthal angles, then used the differencing coefficients and a weighted diamond scheme to calculate the angle derivative term, which added the upstream angular flux to the right hand side of the equation as a known value resulting from solving the starting direction equation due to sweeping order.

We proceeded by applying the DFEM by multiplying the transport equation by a weight function and integrating over the cell volume. We then expanded the angular flux in terms of basis functions. This allowed us to write the matrix form of the DFEM transport equation. Finally, we explained the lumping in the RZ geometry and showed how it enhances the performance of the calculations by localizing the surface, mass, and angle terms calculations at the vertex of the cell.

3. DIFFERENT FEMS RELATED TO PWLD

In this chapter, we describe different spatial discretization methods that are studied in this work. All of them are related to DFEMs or are at least similar. We illustrate the methods using quadrilateral cells of our spherically symmetric grid, but all methods considered here are applicable to general polygonal cells.

3.1 Galerkin PWLD

As illustrated in Figure (3.1), c is the vertex of a quadrilateral cell, $c+1$ and $c-1$ are its counterclockwise and clockwise vertices, respectively. The subcells are triangles that we will call sides, where side s corresponds to vertex c.

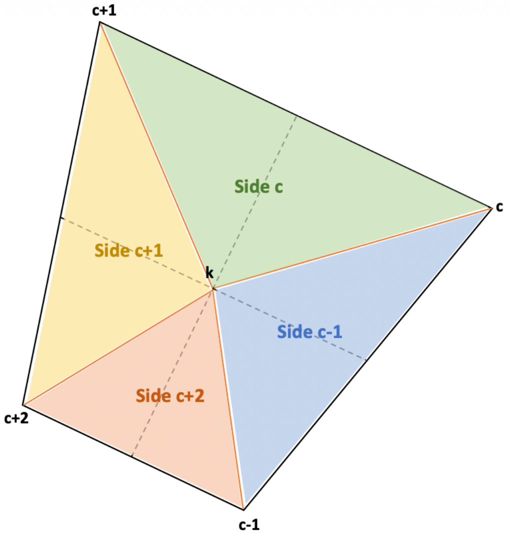

Figure 3.1: Quadrilateral cell and its subcells

In the Galerkin method, the weight function v_i is equal to the PWL basis function b_c.

$$b_c(r,z) = t_c(r,z) + \frac{1}{N}t_k(r,z) \tag{3.1}$$

where t_c is the a linear function that is equal to 1 at the vertex c of the cell and 0 at the other vertices. t_k is the linear function that is equal to 1 at the cell center k and is equal to 0 at the cell vertices.

N is the number of vertices of a cell. The methods developed and studied in this research apply to arbitrary polygonal spatial cells, but the test problems we use have quadrilateral cells, which have $N = 4$. We start with the general form of PWLD transport equation developed in section 2.1 and replace v_i with b_c. Eq (2.20) becomes

$$\begin{aligned}
&\oint_{\partial A} d\ell \hat{e}_n \cdot \hat{\Omega} r b_c \sum_{c'} \tilde{\psi}_{p,q,c'} b_{c'}(r,z) - \iint drdz \left(r \sum_{c'} \psi_{p,q,c'} b_{c'}(r,z) \right) \hat{\Omega} \cdot \vec{\nabla} b_c \\
&\quad + \iint drdz\, b_c \left[\frac{1}{w_{p,q}} \frac{\alpha_{p,q+1/2}}{\tau_{p,q}} \sum_{c'} \psi_{p,q,c'} b_{c'}(r,z) + r\sigma_t \sum_{c'} \psi_{p,q,c'} b_{c'}(r,z) \right] \\
&= \iint drdz\, b_c \left[r \sum_{c'} q_{c'}(r,z) b_{c'}(r,z) + \frac{1}{w_{p,q}} \left(\frac{1-\tau_{p,q}}{\tau_{p,q}} \alpha_{p,q+1/2} + \alpha_{p,q-1/2} \right) \sum_{c'} \psi_{p,q-1/2,c'} b_{c'}(r,z) \right],
\end{aligned} \tag{3.2}$$

The integrals over the area of the cell can be written as a sum of intergrals over the sides of the cell, so Eq. (3.2) can be written as follows,

$$\begin{aligned}
&\sum_e \int_e d\ell \hat{e}_n \cdot \hat{\Omega} r b_c \sum_{c'} \tilde{\psi}_{p,q,c'} b_{c'}(r,z) - \sum_s \iint_s drdz \left(r \sum_{c'} \psi_{p,q,c'} b_{c'}(r,z) \right) \hat{\Omega} \cdot \vec{\nabla} b_c \\
&\quad + \sum_s \iint_s drdz\, b_c \left[\frac{1}{w_{p,q}} \frac{\alpha_{p,q+1/2}}{\tau_{p,q}} \sum_{c'} \psi_{p,q,c'} b_{c'}(r,z) + r\sigma_t \sum_{c'} \psi_{p,q,c'} b_{c'}(r,z) \right] \\
&= \sum_s \iint_s drdz\, b_c \left[r \sum_{c'} q_{c'}(r,z) b_{c'}(r,z) + \frac{1}{w_{p,q}} \left(\frac{1-\tau_{p,q}}{\tau_{p,q}} \alpha_{p,q+1/2} + \alpha_{p,q-1/2} \right) \sum_{c'} \psi_{p,q-1/2,c'} b_{c'}(r,z) \right],
\end{aligned} \tag{3.3}$$

where e is the edge of the cell and s is the side of the cell shown in Fig (3.1). We can expand the surface integral as follows,

$$\sum_e \int_e d\ell \hat{e}_n \cdot \hat{\Omega}_{rz} r b_c \sum_{c'} \psi_{c'} b_{c'} = \sum_{c'} \psi_{c'} \left[\hat{e}_{c+} \cdot \hat{\Omega} \int_{c+} d\ell r b_c b_{c'} + \hat{e}_{c-} \cdot \hat{\Omega} \int_{c-} d\ell r b_c b_{c'} \right] \tag{3.4}$$

where

$$\hat{e}_{c\pm} \cdot \hat{\Omega}_{rz} = \left(\hat{e}^r_{c\pm} + \hat{e}^z_{c\pm} \right) \mu + \left(\hat{e}^r_{c\pm} + \hat{e}^z_{c\pm} \right) \xi, \tag{3.5}$$

and the integrals over edge $c+$ and $c-$ are equal to zero unless $c' = c$ or $c' = c \pm 1$. $\hat{e}^r$ is the unit vector on the r axis and $\hat{e}^z$ is the unit vector on the z axis.

The matrices form of Eq. (3.3) is,

$$\sum_{c'}\left[\mu_{p,q}\left(\mathbf{Lr}^{+}\right)_{c,c'}\tilde{\psi}_{p,q,c'}+\mu_{p,q}\left(\mathbf{Lr}^{-}\right)_{c,c'}\tilde{\psi}_{p,q,c'}+\xi_{p}\left(\mathbf{Lz}^{+}\right)_{c,c'}\tilde{\psi}_{p,q,c'}+\xi_{p}\left(\mathbf{Lz}^{-}\right)_{c,c'}\tilde{\psi}_{p,q,c'}\right]$$
$$+\sum_{c'}\left[\mu_{p,q}\mathbf{Kr}_{c,c'}\psi_{p,q,c'}+\xi_{p}\mathbf{Kz}_{c,c'}\psi_{p,q,c'}+\frac{1}{w_{p,q}}\frac{\alpha_{p,q+1/2}}{\tau_{p,q}}\mathbf{R}_{c,c'}\psi_{p,q,c'}+\sigma_{t}\mathbf{T}_{c,c'}\psi_{p,q,c'}\right]$$
$$=\sum_{c'}\left[\frac{1}{w_{p,q}}\left(\frac{1-\tau_{p,q}}{\tau_{p,q}}\alpha_{p,q+1/2}+\alpha_{p,q-1/2}\right)\mathbf{R}_{c,c'}\psi_{p,q-1/2,c'}+\mathbf{T}_{c,c'}q_{c'}\right] \tag{3.6}$$

The starting direction equation is,

$$\sum_{c'}\left[\mu_{p,1/2}\left(\mathbf{Lr}^{+}\right)_{c,c'}\tilde{\psi}_{p,1/2,c'}+\mu_{p,1/2}\left(\mathbf{Lr}^{-}\right)_{c,c'}\tilde{\psi}_{p,1/2,c'}+\xi_{p}\left(\mathbf{Lz}^{+}\right)_{c,c'}\tilde{\psi}_{p,1/2,c'}+\xi_{p}\left(\mathbf{Lz}^{-}\right)_{c,c'}\tilde{\psi}_{p,1/2,c'}\right]$$
$$+\sum_{c'}\left[\mu_{p,1/2}\left(\mathbf{Kr}_{c,c'}-\mathbf{R}_{c,c'}\right)\psi_{p,1/2,c'}+\xi_{p}\mathbf{Kz}_{c,c'}\psi_{p,1/2,c'}+\sigma_{t}\mathbf{T}_{c,c'}\psi_{p,1/2,c'}\right]=\sum_{c'}\mathbf{T}_{c,c'}q_{c'} \tag{3.7}$$

where

$$\mathbf{T}_{c,c'}=\sum_{s}\iint_{s}dr\,dz\,r\,b_{c}b_{c'} \tag{3.8}$$

$$\mathbf{R}_{c,c'}=\sum_{s}\iint_{s}dr\,dz\,b_{c}b_{c'} \tag{3.9}$$

$$\mathbf{Kr}_{c,c'}=-\sum_{s}\left[\frac{\partial b_{c}}{\partial r}\right]_{s}\iint_{s}dr\,dz\,r\,b_{c'} \tag{3.10}$$

$$\mathbf{Kz}_{c,c'}=-\sum_{s}\left[\frac{\partial b_{c}}{\partial z}\right]_{s}\iint_{s}dr\,dz\,r\,b_{c'} \tag{3.11}$$

$$\left(\mathbf{Lr}^{+}\right)_{c,c'}=\hat{e}_{c+,r}\int_{c}^{c+1}d\ell\,r\,b_{c}\,b_{c'} \tag{3.12}$$

$$\left(\mathbf{Lr}^{-}\right)_{c,c'}=\hat{e}_{c-,r}\int_{c-1}^{c}d\ell\,r\,b_{c}\,b_{c'} \tag{3.13}$$

$$\left(\mathbf{Lz}^{+}\right)_{c,c'}=\hat{e}_{c+,z}\int_{c}^{c+1}d\ell\,r\,b_{c}\,b_{c'} \tag{3.14}$$

$$\left(\mathbf{Lz}^{-}\right)_{c,c'}=\hat{e}_{c-,z}\int_{c-1}^{c}d\ell\,r\,b_{c}\,b_{c'} \tag{3.15}$$

and

$$\left[\frac{\partial b_c}{\partial r}\right]_s = \begin{cases} -\hat{e}_{k\to c+1,r}\frac{\ell_{k\to c+1}}{2A_s} - \hat{e}_{c+,r}\frac{1}{4}\frac{\ell_{c\to c+1}}{2A_s} & \text{for } s = c \\ \hat{e}_{k\to c-1,r}\frac{\ell_{k\to c-1}}{2A_s} - \hat{e}_{c-,r}\frac{1}{4}\frac{\ell_{c\to c-1}}{2A_s} & \text{for } s = c-1 \\ -\hat{e}_{k\to s,r}\frac{1}{4}\frac{\ell_{k\to s}}{2A_s} & \text{otherwise} \end{cases} \tag{3.16}$$

similarly,

$$\left[\frac{\partial b_c}{\partial z}\right]_s = \begin{cases} -\hat{e}_{k\to c+1,z}\frac{\ell_{k\to c+1}}{2A_s} - \hat{e}_{c+,z}\frac{1}{4}\frac{\ell_{c+}}{2A_s} & \text{for } s = c \\ \hat{e}_{k\to c-1,z}\frac{\ell_{k\to c-1}}{2A_s} - \hat{e}_{c-,z}\frac{1}{4}\frac{\ell_{c-}}{2A_s} & \text{for } s = c-1 \\ -\hat{e}_{k\to s,z}\frac{1}{4}\frac{\ell_{k\to s}}{2A_s} & \text{otherwise} \end{cases} \tag{3.17}$$

The subscript $k \to c+1$ represents the edge from the cell center k to the vertex $c+1$, similarly for $k \to c-1$ and $k \to s$ as shown in Fig(3.2).

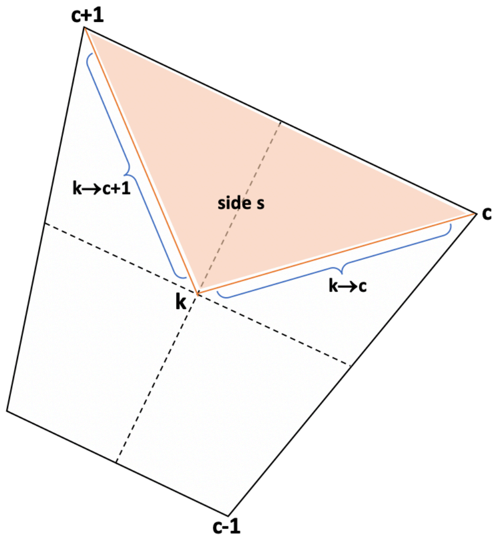

Figure 3.2: Lengths on side s

3.2 Corner Balance PWLD

As illustrated in Figure (3.3), c is the corner index, a corner subcell c is a quadrilateral, $c+1$ and $c-1$ are its counterclockwise and clockwise adjacent subcells, respectively. The figure also shows the surfaces of each subcell indexed as $c\pm$ for the outer surfaces, and $c \pm \frac{1}{2}$ for the inner surfaces.

The Corner Balance method enforces conservation over each corner. We start by integrating

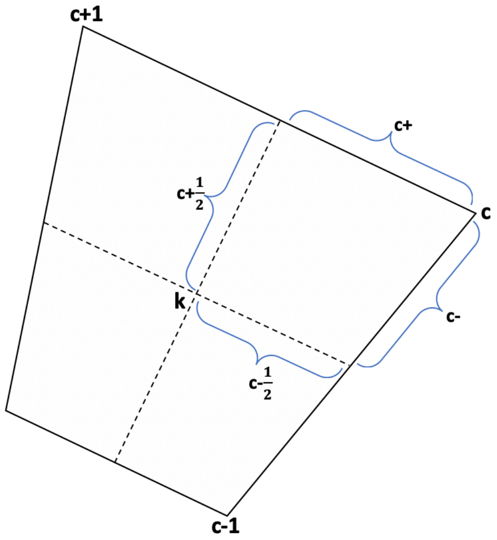

Figure 3.3: Corner c in a quadrilateral cell for the Corner Balance method

the transport equation over the volume of the corner of a cell as follows,

$$\iint_c drdzr\left[\frac{\mu_{p,q}}{r}\frac{\partial(r\psi_{p,q})}{\partial r}+\xi_p\frac{\partial\psi_{p,q}}{\partial z}+\frac{(\alpha\psi)_{p,q+1/2}-(\alpha\psi)_{p,q+1/2}}{rw_{p,q}}+\sigma_t\psi_{p,q}(r,z)-q(r,z)\right]=0, \tag{3.18}$$

or

$$\iint_c drdz\left[\hat{\Omega}\cdot\vec{\nabla}(r\psi_{p,q})+\frac{(\alpha\psi)_{p,q+1/2}-(\alpha\psi)_{p,q+1/2}}{w_{p,q}}+r\sigma_t\psi_{p,q}(r,z)-rq(r,z)\right]=0 \tag{3.19}$$

where c denotes the corner of the cell with

$$\iint_c drdzr=V_c \quad \text{and} \quad \iint_c drdz=A_c \tag{3.20}$$

We apply the Divergence theorem on the gradient term of Eq(3.19),

$$\begin{aligned}\iint_c drdz\hat{\Omega}\cdot\vec{\nabla}(r\psi_{p,q}) &= \int_{c+}d\ell r\hat{e}_{c+}\cdot\hat{\Omega}_{rz}\tilde{\psi}_{p,q}+\int_{c-}d\ell r\hat{e}_{c-}\cdot\hat{\Omega}_{rz}\tilde{\psi}_{p,q}\\ &\quad+\int_{c+1/2}d\ell r\hat{e}_{c+1/2}\cdot\hat{\Omega}_{rz}\psi_{p,q}+\int_{c-1/2}d\ell r\hat{e}_{c-1/2}\cdot\hat{\Omega}_{rz}\psi_{p,q}\end{aligned} \tag{3.21}$$

To obtain the CB-PWLD method, which is a Petrov-Galerkin DFEM, we expand the angular flux in terms of PWL basis functions,

$$\psi_{p,q} = \sum_c \psi_{pq,c} b_c \tag{3.22}$$

We apply the WD definition of $\psi_{p,q+1/2}$ and rearrange Eq.(3.19)

$$\begin{aligned}
&\int_{c+} d\ell r \hat{e}_{c+} \cdot \hat{\Omega}_{rz} \sum_c \tilde{\psi}_{p,q,c} b_c + \int_{c-} d\ell r \hat{e}_{c-} \cdot \hat{\Omega}_{rz} \sum_c \tilde{\psi}_{p,q,c} b_c \\
&+ \int_{c+\frac{1}{2}} d\ell r \hat{e}_{c+\frac{1}{2}} \cdot \hat{\Omega}_{rz} \sum_c \psi_{p,q,c} b_c + \int_{c-\frac{1}{2}} d\ell r \hat{e}_{c-\frac{1}{2}} \cdot \hat{\Omega}_{rz} \sum_c \psi_{p,q,c} b_c \\
&+ \iint_c drdz \left[\frac{1}{w_{p,q}} \frac{\alpha_{p,q+\frac{1}{2}}}{\tau_{p,q}} \sum_c \psi_{p,q,c} b_c + r\sigma_t \sum_c \psi_{p,q,c} b_c \right] \\
&= \iint_c drdz \left[r \sum_c q_c b_c + \frac{1}{w_{p,q}} \left(\frac{1-\tau_{p,q}}{\tau_{p,q}} \alpha_{p,q+\frac{1}{2}} + \alpha_{p,q-\frac{1}{2}} \right) \psi_{p,q-\frac{1}{2},c} b_c \right]
\end{aligned} \tag{3.23}$$

This equation can be written in matrix form,

$$\begin{aligned}
&\sum_{c'} \left[\mu_{p,q} \left(\mathbf{Lr}^{+}\right)_{c,c'} \tilde{\psi}_{p,q,c'} + \mu_{p,q} \left(\mathbf{Lr}^{-}\right)_{c,c'} \tilde{\psi}_{p,q,c'} + \xi_p \left(\mathbf{Lz}^{+}\right)_{c,c'} \tilde{\psi}_{p,q,c'} + \xi_p \left(\mathbf{Lz}^{-}\right)_{c,c'} \tilde{\psi}_{p,q,c'} \right] \\
&+ \sum_{c'} \left[\mu_{p,q} \mathbf{Kr}_{c,c'} \psi_{p,q,c'} + \xi_p \mathbf{Kz}_{c,c'} \psi_{p,q,c'} + \frac{1}{w_{p,q}} \frac{\alpha_{p,q+\frac{1}{2}}}{\tau_{p,q}} \mathbf{R}_{c,c'} \psi_{p,q,c'} + \sigma_t \mathbf{T}_{c,c'} \psi_{p,q,c'} \right] \\
&= \sum_{c'} \left[\mathbf{T}_{c,c'} q_{c'} + \frac{1}{w_{p,q}} \left(\frac{1-\tau_{p,q}}{\tau_{p,q}} \alpha_{p,q+\frac{1}{2}} + \alpha_{p,q-\frac{1}{2}} \right) \mathbf{R}_{c,c'} \psi_{p,q-\frac{1}{2},c'} \right]
\end{aligned} \tag{3.24}$$

where

$$\mathbf{T}_{c,c'} = \iint_c drdz\, r\, b_{c'} \tag{3.25}$$

$$\mathbf{R}_{c,c'} = \iint_c drdz\, b_{c'} \tag{3.26}$$

$$\mathbf{Kr}_{c,c'} = \hat{e}^{r}_{c+\frac{1}{2}} \int_{c+\frac{1}{2}} d\ell r\, b_{c'} + \hat{e}^{r}_{c-\frac{1}{2}} \int_{c-\frac{1}{2}} d\ell r\, b_{c'} \tag{3.27}$$

$$\mathbf{Kz}_{c,c'} = \hat{e}^{z}_{c+\frac{1}{2}} \int_{c+\frac{1}{2}} d\ell r\, b_{c'} + \hat{e}^{z}_{c-\frac{1}{2}} \int_{c-\frac{1}{2}} d\ell r\, b_{c'} \tag{3.28}$$

$$\left(\mathbf{Lr}^{+}\right)_{c,c'} = \hat{e}^{r}_{c+} \int_{c+} d\ell r\, b_{c'} \tag{3.29}$$

$$\left(\mathbf{Lr}^{-}\right)_{c,c'} = \hat{e}^{r}_{c-} \int_{c-} d\ell r \, b_{c'} \tag{3.30}$$

$$\left(\mathbf{Lz}^{+}\right)_{c,c'} = \hat{e}^{z}_{c+} \int_{c+} d\ell r \, b_{c'} \tag{3.31}$$

$$\left(\mathbf{Lz}^{-}\right)_{c,c'} = \hat{e}^{z}_{c-} \int_{c-} d\ell r \, b_{c'} \tag{3.32}$$

3.3 Generalized Corner Balance PWLD

Starting with the corner balance equation,

$$\iint_c dr\, dz\, r \left[\frac{\mu}{r}\frac{\partial(r\psi)}{\partial r} + \frac{\xi}{r}\frac{r\partial\psi}{\partial z} - \frac{1}{r}\frac{\partial(\eta\psi)}{\omega} + \sigma_t \psi - q \right] = 0 \tag{3.33}$$

$$\iint_c dr\, dz\, r\, \hat{\Omega} \cdot \vec{\nabla}_{2D}(r\psi) - \iint_c dr\, dz\, r \frac{\partial(\eta\psi)}{\omega} + \sigma_t \iint_c dr\, dz\, r\psi = \iint_c dr\, dz\, rq \tag{3.34}$$

Applying Gauss divergence theorem,

$$\oint_{\partial c} d\ell\, \hat{\Omega} \cdot \hat{e}_n r \tilde{\psi} - \iint_c dz\, dr \frac{\partial(\eta\psi)}{\omega} + \sigma_t \iint_c dr\, dz\, r\psi = \iint_c dr\, dz\, rq \tag{3.35}$$

$$\sum_e \hat{\Omega} \cdot \hat{e}_{n,e} \int_e d\ell\, r\tilde{\psi} - A_c \left\langle \frac{\partial(\eta\psi)}{\partial\omega} \right\rangle_{cA} + \sigma_t V_c \left\langle \psi \right\rangle_{cV} = V_c \left\langle q \right\rangle_{cV} \tag{3.36}$$

where subscript e represents corner edges and subscript c is the corner. $\tilde{\psi}_e$ is the upstream ψ_e for e on cell edge ($e = c+$ or $c-$), and terms with subscript cA and cV represent the area weighted average and the volume weighted average respectively. We use the same notation for corner edges shown in Fig. (3.3). The corner edges are denoted as $c+$, $c-$, $c+\frac{1}{2}$, and $c-\frac{1}{2}$. The surface area is represented as

$$A_e = \int_e d\ell\, r = \ell_e \left\langle r \right\rangle_e \tag{3.37}$$

where $\langle r\rangle_e$ is the average r along the edge, which equals its value at midpoint. Applying the definition of the area, the corner balance equation becomes

$$\begin{aligned}&\hat{\Omega}\cdot\left[\vec{A}_{c+}\left\langle\tilde{\psi}\right\rangle_{c+}+\vec{A}_{c-}\left\langle\tilde{\psi}\right\rangle_{c-}+\vec{A}_{c+\frac{1}{2}}\langle\psi\rangle_{c+\frac{1}{2}}+\vec{A}_{c-\frac{1}{2}}\langle\psi\rangle_{c-\frac{1}{2}}\right]\\&-A_c\frac{\partial}{\partial\omega}\left(\eta\langle\psi\rangle_{cA}\right)+\sigma_t V_c\langle\psi\rangle_{cV}=V_c\langle q\rangle_{cV}\end{aligned}\tag{3.38}$$

To describe the family of angular flux averages we consider, it is convenient to use the spatial grid shown in Fig.(1.1). If there is no angular discretization error, then for every cell in the same ring (same distance from the origin), we would like for our method to achieve

$$\langle\psi(\Omega_h,\Omega_x)\rangle_{cj}=\text{same for all cells in ring } j=0,...,N_{j-1} \text{ for any given } c=0,1,2,3\tag{3.39}$$

$$\langle\psi(\Omega_h,\Omega_x)\rangle_1=\langle\psi(\Omega_h,-\Omega_x)\rangle_2\tag{3.40}$$

$$\langle\psi(\Omega_h,\Omega_x)\rangle_0=\langle\psi(\Omega_h,-\Omega_x)\rangle_3\tag{3.41}$$

The grid has the following symmetry properties. We define β and γ such that:

$$\begin{aligned}r&=\beta h+\gamma x,\quad h=\beta r+\gamma z\\z&=\gamma h-\beta x,\quad x=\gamma r-\beta z\end{aligned}\tag{3.42}$$

Here $\beta=\sin\theta_j$ and $\gamma=\cos\theta_j$, where θ_j is the rotation angle. The area of corners 1 and 2 are equal, and the areas for corners 0 and 3 are equal.

$$A_0=A_3,\quad A_1=A_2,\tag{3.43}$$

We apply the WD treatment for the angle derivative term,

$$\begin{aligned}-A_c\frac{\partial}{\partial\omega}\left(\eta\Big\langle\psi\Big\rangle_{cA}\right)&=\frac{A_c}{w_{p,q}}\left(\alpha_{p,q+\frac{1}{2}}\Big\langle\psi\Big\rangle_{cA}^{p,q+\frac{1}{2}}-\alpha_{p,q-\frac{1}{2}}\Big\langle\psi\Big\rangle_{cA}^{p,q-\frac{1}{2}}\right)\\&=\frac{A_c}{w_{p,q}}\left[\frac{\alpha_{p,q+\frac{1}{2}}}{\tau_{p,q}}\Big\langle\psi\Big\rangle_{cA}^{p,q}-\left(\frac{1-\tau_{p,q}}{\tau_{p,q}}\alpha_{p,q+\frac{1}{2}}+\alpha_{p,q-\frac{1}{2}}\right)\Big\langle\psi\Big\rangle_{cA}^{p,q-\frac{1}{2}}\right]\end{aligned}\tag{3.44}$$

so the discretized form of Eq.(3.38) for every cell is

$$
\begin{aligned}
&\hat{\Omega}_{p,q}\cdot\left[\vec{A}_{c+}\left\langle\tilde{\psi}\right\rangle_{c+}^{p,q}+\vec{A}_{c-}\left\langle\tilde{\psi}\right\rangle_{c-}^{p,q}+\vec{A}_{c+\frac{1}{2}}\left\langle\psi\right\rangle_{c+\frac{1}{2}}^{p,q}+\vec{A}_{c-\frac{1}{2}}\left\langle\psi\right\rangle_{c-\frac{1}{2}}^{p,q}\right]\\
&+\frac{A_c}{w_{p,q}}\frac{\alpha_{p,q+\frac{1}{2}}}{\tau_{p,q}}\left\langle\psi\right\rangle_{cA}^{p,q+\frac{1}{2}}+\sigma_t V_c\left\langle\psi\right\rangle_{cV}^{p,q}=V_c\left\langle q\right\rangle_{cV}\\
&+\left(\frac{1-\tau_{p,q}}{\tau_{p,q}}\alpha_{p,q+\frac{1}{2}}+\alpha_{p,q-\frac{1}{2}}\right)\left\langle\psi\right\rangle_{cA}^{p,q-\frac{1}{2}}
\end{aligned}
\tag{3.45}
$$

3.4 Simple Corner Balance

The Simple Corner Balance (SCB) method, introduced by Adams [5] and studied by Palmer[7], is defined by the previous equations with the following averages:

$$\left\langle\tilde{\psi}\right\rangle_{c\pm}=\psi_c \tag{3.46}$$

$$\left\langle\psi\right\rangle_{c\pm\frac{1}{2}}=\frac{1}{2}\left(\psi_c+\psi_{c\pm}\right) \tag{3.47}$$

$$\left\langle\psi\right\rangle_{cA}=\left\langle\psi\right\rangle_{cV}=\psi_c \tag{3.48}$$

These definitions localize the mass, outer surface, and angle terms at the vertex of cell, and localize the inner surface of the corner terms at the middle of outer surface. This lumping should improve spherical symmetry.

3.5 Truncation Error

One goal for our method is to achieve second-order truncation error for smooth solutions. We know from previous work [6, 7] that the PWLD method achieves this with either Galerkin or CB weighting, at least in Cartesian-coordinate problems. A formal truncation-error study for the various space-angle discretization combinations we consider in this thesis is beyond the scope of the research, but we have restricted our spatial discretization choices to those that are known to provide second-order solutions in Cartesian-coordinate problems, and thus should provide second-order solutions in cylindrical-coordinate problems if the angle-derivative terms is treated with sufficient accuracy. In Chapter 5 we demonstrate, using manufactured solution, that the methods considered here do in fact achieve second order truncation error on the spherically symmetric spatial grids we employ.

3.6 Diffusion Limit

One goal for our method is to achieve accurate solutions for thick diffusive problems. We have not undertaken a detailed diffusion-limit analysis for all of the candidate methods in this thesis, but we have restricted our spatial-discretization choices to PWLD and CB methods that have been shown to have the desired diffusion-limit behavior in Cartesian-coordinate problems[5, 8]. Todd Palmer [7] included thick diffusion analysis for SCB method as well as "Bilinear Discontinuous" (BLD) method which is closely related to PWLD.

3.7 Demonstration

In this section, we explain that we can not hope for symmetry in a transport problem if we do not get it when we have only the collision and source terms. We simply project a symmetric function onto the PWLD basis in a single cell, the solutions that are symmetric in x are those that depend only on h, meaning $\psi_1 = \psi_2$ and $\psi_0 = \psi_3$. For example, we define $f(h) = h^2 + x^2$. We solve for corner 1 and 2 to show whether they are equal. For CB-PWLD, the weight function v_c is 1 so the following equation needs to be satisfied to get symmetry,

$$\iint_c dxdh\,(\beta h + \gamma x)\sum_{c'} \psi_{c'} b_{c'} = \iint_c dxdh\,(\beta h + \gamma x)\,(h^2 + x^2) \tag{3.49}$$

Assuming $\psi_1 = \psi_2$, and $\psi_0 = \psi_3$

$$\sum_{c'} \psi_{c'} b_{c'} = \psi_{min}\frac{h_{max} - h}{\Delta h} + \psi_{max}\frac{h - h_{min}}{\Delta h} \tag{3.50}$$

where the subscript min means corners 0 and 3 and subscript max means corners 1 and 2. The left hand side of Eq.(3.49) for corner 1 or 0 is written as follows

$$\begin{aligned}\text{LHS} &= \frac{1}{\Delta h}\int_{h_l}^{h_u} dh \int_{0}^{\alpha h} (\beta h + \gamma x)\left[\psi_{min}(h_{max} - h) + \psi_{max}(h - h_{min})\right] \\ &= \frac{1}{\Delta h}\left(\beta\alpha + \frac{1}{2}\gamma\alpha^2\right)\left[(\psi_{min}h_{max} - \psi_{max}h_{min})\frac{h_u^3 - h_l^3}{3} + (\psi_{max} - \psi_{min})\frac{h_u^4 - h_l^4}{4}\right]\end{aligned} \tag{3.51}$$

where h_u and h_l are the upper and lower h values for each corner, and α is a constant

$$\alpha = x_{min}/h_{min} \text{ or } x_{max}/h_{max} \tag{3.52}$$

Similarly for corner 2 or 3,

$$\begin{aligned}\text{LHS} &= \frac{1}{\Delta h}\int_{h_l}^{h_u} dh \int_{-\alpha h}^{0} (\beta h + \gamma x)\left[\psi_{min}(h_{max} - h) + \psi_{max}(h - h_{min})\right] \\ &= \frac{1}{\Delta h}\left(\beta\alpha - \frac{1}{2}\gamma\alpha^2\right)\left[(\psi_{min}h_{max} - \psi_{max}h_{min})\frac{h_u^3 - h_l^3}{3} + (\psi_{max} - \psi_{min})\frac{h_u^4 - h_l^4}{4}\right]\end{aligned} \tag{3.53}$$

The right hand side for Eq.(3.49) for corner 1 or 0

$$\begin{aligned}\text{RHS} &= \int_{h_l}^{h_u} dh \int_{0}^{\alpha h} (\beta h + \gamma x)(h^2 + x^2) \\ &= \frac{1}{5}\left(h_u^5 - h_l^5\right)\left(\beta\alpha + \frac{1}{2}\gamma\alpha^2 + \frac{1}{3}\beta\alpha^3 + \frac{1}{4}\gamma\alpha^4\right)\end{aligned} \tag{3.54}$$

and for corner 2 or 3

$$\begin{aligned}\text{RHS} &= \int_{h_l}^{h_u} dh \int_{-\alpha h}^{0} (\beta h + \gamma x)(h^2 + x^2) \\ &= \frac{1}{5}\left(h_u^5 - h_l^5\right)\left(\beta\alpha - \frac{1}{2}\gamma\alpha^2 + \frac{1}{3}\beta\alpha^3 - \frac{1}{4}\gamma\alpha^4\right)\end{aligned} \tag{3.55}$$

Since h_u is the same for corners 1 and 2, and h_l is at the cell center, we can combine equations (3.51)-(3.55)

$$\left[a(h_x^3 - h_k^3) + b(h_x^4 - h_k^4)\right]\left(\beta \pm \frac{\gamma\alpha}{2}\right) = \left(h_x^5 - h_k^5\right)\left[\beta\left(1 + \frac{\alpha^2}{3}\right) \pm \frac{\gamma\alpha}{2}\left(1 + \frac{\alpha^2}{2}\right)\right] \quad (3.56)$$

$$\left[a(h_k^3 - h_n^3) + b(h_k^4 - h_n^4)\right]\left(\beta \pm \frac{\gamma\alpha}{2}\right) = \left(h_k^5 - h_n^5\right)\left[\beta\left(1 + \frac{\alpha^2}{3}\right) \pm \frac{\gamma\alpha}{2}\left(1 + \frac{\alpha^2}{2}\right)\right] \quad (3.57)$$

where h_x is the value of h corresponding to corners 1 and 2, h_k is the value of h at the cell center, and h_n is the value of h corresponding to corners 0 and 3. The positive γ terms are for corners 0 and 1, and the negative γ terms are for corners 2 and 3. If the factors $\left(1 + \frac{\alpha^2}{2}\right)$ and $\left(1 + \frac{\alpha^2}{3}\right)$ were the same, then LHS and RHS would be the same and a symmetric solution would hold, but this is not the case. So CB-PWLD will not retain symmetry.

Next we show the projection of the function $f(h) = h^2 + x^2$ using G-PWLD where $v_i = b_c$. To get symmetry we need

$$\iint_{cell} drdz\, rb_c \sum_{c'} \psi_{c'} c_{c'} = \iint_{cell} drdz\, rb_c(r^2 + z^2) \quad (3.58)$$

Note that

$$b_0 + b_3 = \frac{h_x - h}{h_x - h_n} \quad (3.59)$$

$$b_1 + b_2 = \frac{h - h_n}{h_x - h_n} \quad (3.60)$$

and

$$b_0 - b_3 = \begin{cases} g_0(h, x) & x > 0 \\ -g_0(h, x) & x < 0 \end{cases} \quad (3.61)$$

$$b_1 - b_2 = \begin{cases} g_1(h, x) & x > 0 \\ -g_1(h, x) & x < 0 \end{cases} \quad (3.62)$$

The four equations of the corners can be replaced by the following equivalent system

$$\int_{h_n}^{h_x} dh \int_{-\alpha h}^{\alpha h} (\beta h + \gamma x)(b_0 + b_3) \sum_{c'} \psi_{c'} b_{c'} = \int_{h_n}^{h_x} dh \int_{-\alpha h}^{\alpha h} dx (\beta h + \gamma x)(b_0 + b_3)(h^2 + x^2) \quad (3.63)$$

$$\int_{h_n}^{h_x} dh \int_{-\alpha h}^{\alpha h} (\beta h + \gamma x)(b_1 + b_2) \sum_{c'} \psi_{c'} b_{c'} = \int_{h_n}^{h_x} dh \int_{-\alpha h}^{\alpha h} dx (\beta h + \gamma x)(b_1 + b_2)(h^2 + x^2) \quad (3.64)$$

$$\int_{h_n}^{h_x} dh \int_{-\alpha h}^{\alpha h} (\beta h + \gamma x)(b_0 - b_3) \sum_{c'} \psi_{c'} b_{c'} = \int_{h_n}^{h_x} dh \int_{-\alpha h}^{\alpha h} dx (\beta h + \gamma x)(b_0 - b_3)(h^2 + x^2) \quad (3.65)$$

$$\int_{h_n}^{h_x} dh \int_{-\alpha h}^{\alpha h} (\beta h + \gamma x)(b_1 - b_2) \sum_{c'} \psi_{c'} b_{c'} = \int_{h_n}^{h_x} dh \int_{-\alpha h}^{\alpha h} dx (\beta h + \gamma x)(b_1 - b_2)(h^2 + x^2) \quad (3.66)$$

We insert the desired symmetry $\psi_1 = \psi_2$ and $\psi_3 = \psi_0$ to see if it contradicts the 4 equations. Starting with Eq.(3.63)

$$\int_{h_n}^{h_x} dh \int_{-\alpha h}^{\alpha h} (\beta h + \gamma x)(b_0 + b_3) \left[\psi_0(b_0 + b_3) + \psi_1(b_1 + b_2)\right] = \int_{h_n}^{h_x} dh \int_{-\alpha h}^{\alpha h} dx (\beta h + \gamma x)(b_0 + b_3)(h^2 + x^2) \quad (3.67)$$

since all terms multiplied by γx integrate to zero because $(b_0 + b_3)$ is even, we get

$$\int_{h_n}^{h_x} dh \beta h (b_0 + b_3) \left[\psi_0(b_0 + b_3) + \psi_1(b_1 + b_2)\right] 2\alpha h = \int_{h_n}^{h_x} dh \beta h (b_0 + b_3) \left(2\alpha h^3 + \frac{2}{3}\alpha^3 h^3\right) \quad (3.68)$$

Similarly, Eq.(3.64) becomes

$$\int_{h_n}^{h_x} dh \beta h (b_1 + b_2) \left[\psi_0(b_0 + b_3) + \psi_1(b_1 + b_2)\right] 2\alpha h = \int_{h_n}^{h_x} dh \beta h (b_1 + b_2) \left(2\alpha h^3 + \frac{2}{3}\alpha^3 h^3\right) \quad (3.69)$$

So Eq.(3.68) and (3.69) completely determine ψ_1 and ψ_0. Let $f_0 = b_0 + b_3$ and $f_1 = b_1 + b_2$, Eq.(3.68) and (3.69) become

$$\int_{h_n}^{h_x} dh h^2 f_0 \left[\psi_0 f_0 + \psi_1 f_1\right] = \int_{h_n}^{h_x} dh h^4 f_0 \left(1 + \frac{\alpha^2}{3}\right) \quad (3.70)$$

$$\int_{h_n}^{h_x} dh h^2 f_1 \left[\psi_0 f_0 + \psi_1 f_1\right] = \int_{h_n}^{h_x} dh h^4 f_1 \left(1 + \frac{\alpha^2}{3}\right) \tag{3.71}$$

Now we check if Eq.(3.65) and (3.66) are satisfied. Starting with Eq.(3.65)

$$\int_{h_n}^{h_x} dh \int_{-\alpha h}^{\alpha h} (\beta h + \gamma x)(b_0 - b_3)\left[\psi_0(b_0 + b_3) + \psi_1(b_1 + b_2)\right] = \int_{h_n}^{h_x} dh \int_{-\alpha h}^{\alpha h} dx (\beta h + \gamma x)(b_0 - b_3)(h^2 + x^2) \tag{3.72}$$

since $b_0 - b_3$ is odd in x, after integration we get

$$\int_{h_n}^{h_x} dh \left[\psi_0 f_0 + \psi_1 f_1\right] \int_{-\alpha h}^{\alpha h} dx x(b_0 - b_3) = \int_{h_n}^{h_x} dh \int_{-\alpha h}^{\alpha h} dx\, x(b_0 - b_3)(h^2 + x^2) \tag{3.73}$$

Similarly, Eq.(3.66) is

$$\int_{h_n}^{h_x} dh \left[\psi_0 f_0 + \psi_1 f_1\right] \int_{-\alpha h}^{\alpha h} dx x(b_1 - b_2) = \int_{h_n}^{h_x} dh \int_{-\alpha h}^{\alpha h} dx\, x(b_1 - b_2)(h^2 + x^2) \tag{3.74}$$

From Eq.(3.73) we have 2 integrals in x,

$$I_1 = \int_{-\alpha h}^{\alpha h} dx\, x(b_0 - b_3) \tag{3.75}$$

$$I_3 = \int_{-\alpha h}^{\alpha h} dx\, x^3(b_0 - b_3) \tag{3.76}$$

and we have the same two integrals but with $b_1 - b_2$ from Eq.(3.74). So the only way we can get ψ_0 and ψ_1 to satisfy the equations is if

$$\frac{I_3}{I_1} = \frac{\alpha^2}{3} \tag{3.77}$$

Otherwise, the value would not be consistent with the values defined in Eq.(3.68) and (3.69). Continuing with some algebra that is not included, we confirmed that $\frac{I_3}{I_1} \neq \frac{\alpha^2}{3}$. So G-PWLD does not produce a symmetric solution in x.

In SCB, the equation that needs to be satisfied is

$$V_c \langle \psi \rangle_{cV} = \underbrace{\iint_c dx dh \left(\beta h + \gamma x\right)}_{V_c} \left(h^2 + x^2\right) \tag{3.78}$$

In the right hand side, the integral is equal to V_c, and on the left hand side $\langle \psi \rangle_{cV}$ is evaluated at the vertex of the corner, Eq.(3.78) becomes

$$V_c \psi_c = V_c \left(h_c^2 + x_c^2\right) \tag{3.79}$$

$$\psi_c = \left(h_c^2 + x_c^2\right) \tag{3.80}$$

So SCB will retain symmetry.

4. ANGLE DISCRETIZATION METHODS

4.1 Discussion on Collocation

The standard treatment of the angle-derivative term in the cylindrical-geometry discrete-ordinates transport equation can be viewed as a collocation method, in which the equation is required to hold only at each quadrature direction. In this treatment the spatial-derivative and collision terms are evaluated at quadrature directions, and the angle-derivative term is approximated such that the method is exact when the solution is constant in the spatial and angular variables.

Each collocation equation can be viewed as a conservation equation: if we integrate over the azimuthal-angle bin associated with the quadrature point, then we can approximate the resulting angle-averaged quantities in such a way that we obtain the collocated equations. From this perspective, the approximations of the averaged quantities appear to be inaccurate, meaning the resulting equation might not be accurate for a given angle bin. However, from the point of view of collocation (as opposed to bin-wise conservation), the standard treatment should produce accurate approximations to integrals over the full angular range (including accurate conservation over the full range), even though the equation at each point might not accurately approximate conservation over its angle bin.

An alternative treatment of the angle-derivative term is to integrate the equation over the azimuthal-angle range associated with each quadrature point and then more accurately approximate the averaged quantities in the resulting conservation equation. With such a treatment, bin-wise conservation should be improved. Perhaps more importantly, the angle-derivative term would be treated much like the spatial-derivative terms, with conservation imposed cell-wise and bin-wise. The potential down side is that full-range angular integrations might be less accurate. Depending on how the angle-averaged quantities are approximated, the alternative treatment might degrade accuracy in diffusive problems (for example, by yielding an effective diffusion coefficient different from $1/(3\sigma_t)$).

In this chapter we introduce candidate discretizations based on integrating the transport equation over each azimuthal angle bin for each polar quadrature direction.

4.2 Diamond Differencing Like Method

In Chapter 2, we used a weighted diamond difference scheme to calculate $\psi_{p,q+\frac{1}{2}}(r,z)$. This approximation preserves a linear solution in $\cos(\omega)$, which is also linear in x of the coordinate system shown in Fig(4.1). However, the variation in y is ignored which violates causality since the downstream value depends more on values that are transverse than those that are upstream. This is especially problematic if we consider the case of 2 azimuthal quadrature points. So we seek an alternative to the weighted diamond difference that better represents the physical dependence of $\psi_{p,q+\frac{1}{2}}(r,z)$ on the incoming $\psi_{p,q}(r,z)$ and $\psi_{p,q-\frac{1}{2}}(r,z)$.

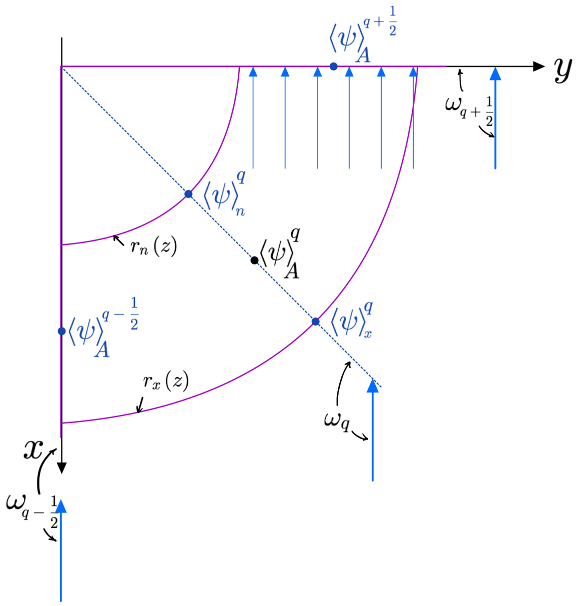

Figure 4.1: Top view of flow in one direction.

Starting with the Corner Balance equation, without spatial approximation

$$\sum_{f=c\pm,c\pm\frac{1}{2}} \hat{\Omega}_{p,q}\cdot\vec{A}_f\left\langle\tilde{\psi}\right\rangle_f^{p,q} + A_c\frac{\alpha_{p,q+\frac{1}{2}}\left\langle\psi\right\rangle_{cA}^{p,q+\frac{1}{2}} - \alpha_{p,q-1/2}\left\langle\psi\right\rangle_{cA}^{p,q-\frac{1}{2}}}{w_{p,q}} + \sigma_t V_c\left\langle\psi\right\rangle_{cV}^{p,q} = V_c\left\langle q\right\rangle_c \quad (4.1)$$

We re-interpret the CB equation as an integral over a 3D spatial volume with a fixed $\hat{\Omega}$ divided by

$\Delta\omega_{p,q}$:

$$V_c \left\langle \psi \right\rangle_{p,q}^{cV} = \frac{1}{\Delta\omega_{p,q}} \iint_c dr dz\, r \int_{\omega_{p,q-\frac{1}{2}}}^{\omega_{p,q+\frac{1}{2}}} d\omega\, \psi = \frac{1}{\Delta\omega_{p,q}} \iiint_{c\Delta\omega} dx dy dz\, \psi \tag{4.2}$$

$$\begin{aligned}\sum_{\substack{f=c\pm,c\pm\frac{1}{2}\\ q\pm\frac{1}{2}}} \hat{\Omega}_{p,q} \cdot \vec{A}_f \left\langle \tilde{\psi} \right\rangle_f^{p,q} &= \sum_{f=c\pm,c\pm\frac{1}{2}} \left[\xi_p e_f^z + (1-\xi_p^2)^{\frac{1}{2}} \left\langle \cos(\omega) \right\rangle_{p,q} e_f^r \right] \vec{A}_f \left\langle \tilde{\psi} \right\rangle_f^{p,q} \\ &+ \frac{(1-\xi_p^2)^{\frac{1}{2}}}{\Delta\omega_{p,q}} \left[\left(\sin(\omega) \left\langle \psi \right\rangle_A\right)_{p,q+\frac{1}{2}} - \left(\sin(\omega) \left\langle \psi \right\rangle_A\right)_{p,q-\frac{1}{2}} \right]\end{aligned} \tag{4.3}$$

where

$$\left\langle \cos(\omega) \right\rangle_{p,q} = \underbrace{\left[\frac{\sin(\frac{\Delta\omega_{p,q}}{2})}{\Delta\omega_{p,q}/2} \right]}_{\lambda_{p,q}} \cos(\omega)_{p,q} \tag{4.4}$$

Applying the new ratio $\lambda_{p,q}$ to the differencing coefficients and $\hat{\Omega}$

$$\begin{gathered} \alpha_{p,q+\frac{1}{2}} = \alpha_{p,q-\frac{1}{2}} - w_{p,q}\mu_{p,q}\lambda_{p,q} \\ \hat{\Omega}_{p,q} = \xi_p \hat{e}_z + \mu_{p,q}\lambda_{p,q}\hat{e}_r \end{gathered} \tag{4.5}$$

Eq.(4.3) can be rewritten as follows,

$$\sum_{\substack{f=c\pm,c\pm1/2\\ q\pm1/2}} \hat{\Omega}_{p,q} \cdot \vec{A}_f \left\langle \tilde{\psi} \right\rangle_f^{p,q} = \sum_{\text{exit } f} \epsilon_f^{p,q} \left\langle \psi \right\rangle_f^{p,q} - \sum_{\text{inc } f} \nu_f^{p,q} \left\langle \psi \right\rangle_f^{p,q} \tag{4.6}$$

where

$$
\begin{aligned}
\epsilon_f^{p,q}\Big|_{f=q+\frac{1}{2}} &= \frac{A_c}{w_{p,q}}\alpha_{p,q+\frac{1}{2}} \\
\nu_f^{p,q}\Big|_{f=q-\frac{1}{2}} &= \frac{A_c}{w_{p,q}}\alpha_{p,q-\frac{1}{2}} \\
\hat{\Omega}_{p,q}\cdot\vec{A}_{c\pm} &= \begin{cases} \epsilon_{c\pm}^{p,q}, & \hat{\Omega}_{p,q}\cdot\vec{A}_{c\pm} > 0, \\ -\nu_{c\pm}^{p,q}, & \hat{\Omega}_{p,q}\cdot\vec{A}_{c\pm} < 0, \end{cases} \\
\hat{\Omega}_{p,q}\cdot\vec{A}_{c\pm\frac{1}{2}} &= \begin{cases} \epsilon_{c\pm\frac{1}{2}}^{p,q}, & \hat{\Omega}_{p,q}\cdot\vec{A}_{c\pm\frac{1}{2}} > 0, \\ -\nu_{c\pm\frac{1}{2}}^{p,q}, & \hat{\Omega}_{p,q}\cdot\vec{A}_{c\pm\frac{1}{2}} < 0, \end{cases}
\end{aligned}
\tag{4.7}
$$

Our new diamond difference-like technique makes the following approximation

$$\langle\psi\rangle_{cA}^{p,q} \approx \frac{1}{2}\bigg[\langle\psi\rangle_{\text{exit}}^{p,q} - \langle\psi\rangle_{\text{inc}}^{p,q}\bigg] \tag{4.8}$$

where the incident and exiting averages of the angular flux are weighted by the fraction they contribute to the total inflow and outflow as follows

$$
\begin{aligned}
\langle\psi\rangle_{\text{exit}}^{p,q} &= \frac{\sum_{\text{exit } f}\epsilon_f^{p,q}\langle\psi\rangle_f^{p,q}}{\sum_{\text{exit } f}\epsilon_f^{p,q}} \\
\langle\psi\rangle_{\text{inc}}^{p,q} &= \frac{\sum_{\text{inc } f}\nu_f^{p,q}\langle\psi\rangle_f^{p,q}}{\sum_{\text{inc } f}\epsilon_f^{p,q}}
\end{aligned}
\tag{4.9}
$$

Since the projected area perpendicular to $\hat{\Omega}$ of the incident faces of the cell has to be equal to the area of the exiting faces of the cell,

$$\sum_{\text{exit } f}\epsilon_f^{p,q} = \sum_{\text{inc } f}\nu_f^{p,q} = A_{c,pro}^{p,q} \tag{4.10}$$

the CB equation with diamond difference-like approximation becomes

$$2A_{c,pro}^{p,q}\langle\psi\rangle_{cA}^{p,q} + \sigma_t V_c\langle\psi\rangle_{cV}^{p,q} = V_c\langle q\rangle_c + 2\sum_{\text{inc } f}\nu_f^{p,q}\langle\psi\rangle_f^{p,q} \tag{4.11}$$

Using the lumped version makes $\langle\psi\rangle_{cA} = \langle\psi\rangle_{cV}$, so we can solve for the corner averaged flux in terms of incident flux and volumetric source,

$$\left[2A^{p,q}_{c,pro} + \sigma_t V_c\right] \langle\psi\rangle^{p,q}_{cV} = V_c \langle q\rangle_c + 2\sum_{\text{inc } f} \nu^{p,q}_f \langle\psi\rangle^{p,q}_f \tag{4.12}$$

Note that the starting direction is not needed anymore because it does not contribute any incident particles since $\alpha_{p,\frac{1}{2}} = 0$.

Next, we can solve for $\langle\psi\rangle^{p,q+\frac{1}{2}}_c$ by applying Eq. (4.8) to the CB equation (4.1) ,

$$\begin{aligned} \frac{A_c}{w_{p,q}} \alpha_{p,q+\frac{1}{2}} \langle\psi\rangle^{p,q+\frac{1}{2}}_{cA} &= \frac{A_c}{w_{p,q}} \left[\left(\alpha_{p,q+\frac{1}{2}} + \alpha_{p,q-\frac{1}{2}}\right) \langle\psi\rangle^{p,q}_{cA} - \alpha_{p,q-\frac{1}{2}} \langle\psi\rangle^{p,q-\frac{1}{2}}_{cA} \right] \\ + \sum_{\substack{\text{exit} \\ f\in\left(c\pm, c\pm\frac{1}{2}\right)}} \epsilon^{p,q}_f &\left[\langle\psi\rangle^{p,q}_{cA} - \langle\psi\rangle^{p,q}_f \right] + \sum_{\substack{\text{inc} \\ f\in\left(c\pm, c\pm\frac{1}{2}\right)}} \nu^{p,q}_f \left[\langle\psi\rangle^{p,q}_{cA} - \langle\psi\rangle^{p,q}_f \right] \end{aligned} \tag{4.13}$$

Note that when $\alpha_{p,q+\frac{1}{2}} = 0$, we do not need to apply the diamond difference-like method, and the CB equation is written as follows,

$$\begin{aligned} \sum_{f=c\pm\frac{1}{2}} \hat{\Omega}_{p,q} \cdot \vec{A}_f \langle\psi\rangle^{p,q}_f + \sum_{\text{exit } f=c\pm} \hat{\Omega}_{p,q} \cdot \vec{A}_f \langle\psi\rangle^{p,q}_f + \sigma_t V_c \langle\psi\rangle^{p,q}_{cV} = V_c \langle q\rangle_c \\ - \sum_{\text{inc } f=c\pm} \hat{\Omega}_{p,q} \cdot \vec{A}_f \langle\psi\rangle^{p,q}_f + A_c \frac{\alpha_{p,q-1/2}}{w_{p,q}} \langle\psi\rangle^{p,q-\frac{1}{2}}_{cA} \end{aligned} \tag{4.14}$$

This method does not improve the symmetry as much as we hope, so we extend the idea of treating the angle derivative term the same way we treat the spatial derivative term, and we explore a three-dimensional balance method.

4.3 Multiple Balance Method

The Multiple Balance (MB) method uses a different approximation, that depend on the outgoing half range of the azimuthal angle domain $\omega \in (\omega_q, \omega_{q+\frac{1}{2}})$. We use the lumped version of the CB equation where the volume, area, and surface terms are localized at the corner vertex.

Starting with the CB equation,

$$\sum_{f=c\pm,c\pm\frac{1}{2}} \hat{\Omega}_{p,q}\cdot\vec{A}_f \left\langle\tilde{\psi}\right\rangle_f^{p,q} + A_c \frac{\alpha_{p,q+\frac{1}{2}}\left\langle\psi\right\rangle_{cA}^{p,q+\frac{1}{2}} - \alpha_{p,q-1/2}\left\langle\psi\right\rangle_{cA}^{p,q-\frac{1}{2}}}{w_{p,q}} + \sigma_t V_c \left\langle\psi\right\rangle_{cV}^{p,q} = V_c \left\langle q\right\rangle_c \tag{4.15}$$

we integrate over the aforementioned half range $\omega \in (\omega_q, \omega_{q+\frac{1}{2}})$,

$$\sum_{f=c\pm,c\pm\frac{1}{2}} \hat{\Omega}_{p,q+\frac{1}{4}}\cdot\vec{A}_f \left\langle\tilde{\psi}\right\rangle_f^{p,q+\frac{1}{4}} + A_c \frac{\alpha_{p,q+\frac{1}{2}}\left\langle\psi\right\rangle_{cA}^{p,q+\frac{1}{2}} - \alpha_{p,q}\left\langle\psi\right\rangle_{cA}^{p,q}}{w_{p,q}} + \sigma_t V_c \left\langle\psi\right\rangle_{cV}^{p,q+\frac{1}{2}} = V_c \left\langle q\right\rangle_c \tag{4.16}$$

where

$$\alpha_{p,q} = \alpha_{p,q+\frac{1}{2}} + w_{p,q}\mu_{p,q+\frac{1}{4}}\lambda_{p,q+\frac{1}{4}} \tag{4.17}$$

$$\hat{\Omega}_{p,q+\frac{1}{4}} = \xi_p \hat{e}_z + \mu_{p,q+\frac{1}{4}}\lambda_{p,q+\frac{1}{4}}\hat{e}_r \tag{4.18}$$

$$\lambda_{p,q+\frac{1}{4}} = \begin{cases} \frac{4\sin(\frac{\Delta\omega_{p,q}}{4})}{\Delta\omega_{p,q}} & \text{using bin-wise approximation} \\ 1 & \text{using collocation} \end{cases} \tag{4.19}$$

We must define the averages that appear in this half-range balance equation. If we are using SCB for the full range balance equation we also use it here and we evaluate our terms on the outflow surface $q+\frac{1}{2}$. This produces:

$$\left\langle\tilde{\psi}\right\rangle_{c\pm}^{p,q+\frac{1}{4}} = \begin{cases} \psi_c^{p,q+\frac{1}{2}}, & \hat{\Omega}_{p,q}\cdot\vec{A}_{c\pm} > 0 \text{ or } \hat{\Omega}_{p,q+\frac{1}{4}}\cdot\vec{A}_{c\pm} > 0 \\ \tilde{\psi}_{\text{inc } c\pm}^{p,q+\frac{1}{2}}, & \text{otherwise} \end{cases} \tag{4.20}$$

$$\left\langle\tilde{\psi}\right\rangle_{c\pm\frac{1}{2}}^{p,q+\frac{1}{4}} = \frac{1}{2}\left(\psi_c^{p,q+\frac{1}{2}} + \psi_{c\pm1}^{p,q+\frac{1}{2}}\right) \tag{4.21}$$

Note that the expression on the $c\pm\frac{1}{2}$ surfaces couples all of the corner quantities at $q+\frac{1}{2}$, and of course they are also coupled to the corner quantities at q. We seek an approximation that decouples the $q+\frac{1}{2}$ quantities, and we try the following:

$$\left\langle \tilde{\psi} \right\rangle_{c\pm\frac{1}{2}}^{p,q+\frac{1}{4}} \approx \psi_c^{p,q+\frac{1}{2}} + \frac{1}{2}\left(\psi_{c\pm1}^{p,q} - \psi_c^{p,q}\right) \tag{4.22}$$

The definitions of the angular on the corner surfaces are made such that $\psi_c^{p,q+\frac{1}{2}}$ is not coupled to $\psi_{c'}^{p,q+\frac{1}{2}}$ when $c' \neq c$. Note that the incident and exiting treatment is determined by $\hat{\Omega}_{p,q} \cdot \vec{A}_{c\pm}$ for the whole 3D volume, knowing that $c\pm$ surfaces often have incoming and outgoing portions. Applying these approximations result in the following equation for $\psi_c^{p,q+\frac{1}{2}}$,

$$\begin{aligned}
&\left[\sum_{\text{exit } f=c\pm} \hat{\Omega}_{p,q+\frac{1}{4}} \cdot \vec{A}_f + \sum_{f=c\pm\frac{1}{2}} \hat{\Omega}_{p,q+\frac{1}{4}} \cdot \vec{A}_f + 2A_c \frac{\alpha_{p,q+\frac{1}{2}}}{w_{p,q}} + \sigma_t V_c\right] \psi_c^{p,q+\frac{1}{2}} \\
&= \sum_{\text{inc } f=c\pm} \left(-\hat{\Omega}_{p,q+\frac{1}{4}} \cdot \vec{A}_f\right) \tilde{\psi}_f^{p,q+\frac{1}{2}} + \sum_{f=c\pm\frac{1}{2}} \hat{\Omega}_{p,q+\frac{1}{4}} \cdot \vec{A}_f \frac{1}{2}\left(\psi_c^{p,q} - \psi_{c\pm1}^{p,q}\right) \\
&\quad + 2A_c \frac{\alpha_{p,q}}{w_{p,q}} \psi_c^{p,q} + V_c q_c
\end{aligned} \tag{4.23}$$

Next, we insert the expression of $\psi_c^{p,q+\frac{1}{2}}$ from Eq. (4.23) into the CB equation,

$$\begin{aligned}
&\sum_{\text{exit } f=c\pm} \hat{\Omega}_{p,q} \cdot \vec{A}_f \left\langle \psi \right\rangle_f^{p,q} + \sum_{f=c\pm\frac{1}{2}} \left[\hat{\Omega}_{p,q} \cdot \vec{A}_f \left\langle \psi \right\rangle_f^{p,q} + \gamma_c^{p,q} \hat{\Omega}_{p,q+\frac{1}{4}} \cdot \vec{A}_f \frac{1}{2}\left(\psi_c^{p,q} - \psi_{c\pm1}^{p,q}\right)\right] \\
&\quad + 2\gamma_c^{p,q} A_c \frac{\alpha_{p,q}}{w_{p,q}} \psi_c^{p,q} + \sigma_t V_c \left\langle \psi \right\rangle_c^{p,q} = V_c \left\langle q \right\rangle_c \left(1 - \gamma_c^{p,q}\right) \\
&+ \sum_{\text{inc } f=c\pm} \left[-\left(\hat{\Omega}_{p,q} \cdot \vec{A}_f\right) \left\langle \tilde{\psi} \right\rangle_f^{p,q} + \gamma_c^{p,q} \hat{\Omega}_{p,q+\frac{1}{4}} \cdot \vec{A}_f \left\langle \tilde{\psi} \right\rangle_f^{p,q+\frac{1}{4}}\right] + A_c \frac{\alpha_{p,q-\frac{1}{2}}}{w_{p,q}} \psi_c^{p,q-\frac{1}{2}}
\end{aligned} \tag{4.24}$$

where

$$\gamma_c^{p,q} = \frac{\alpha_{p,q+\frac{1}{2}}}{w_{p,q}} \frac{A_c}{d_c^{p,q+\frac{1}{2}}} \tag{4.25}$$

and $d_c^{p,q+\frac{1}{2}}$ is the left hand side coefficient of Eq.(4.23).

5. NUMERICAL RESULTS

5.1 Simple Spherical Test Problem

First we introduce a manufactured spherical solution,

$$\psi_{sph}(\rho, \mu_{sph})) = \frac{1}{2\pi}\left[\phi_0 + \rho^2\phi_r\right] - \frac{2\phi_r}{\sigma_t}\rho\mu_{sph} \tag{5.1}$$

where ϕ_0 and ϕ_r are arbitrary constants. When mapped onto cylindrical coordinates, Eq. (5.1) is written as follows

$$\psi_{inc1}(r, z, \mu, \xi) = \frac{1}{2\pi}\left[\phi_0 + \left(r^2 + z^2\right)\phi_r\right] - \frac{2\phi_r}{\sigma_t}\left(z\xi + r\mu\right) \tag{5.2}$$

$$\phi(r, z) = \phi_0 + (r^2 + z^2)\phi_r \tag{5.3}$$

The scalar flux in this problem is a function of only ρ the distance from the origin which makes it spherically symmetric. We apply the solution to the transport equation terms

$$2\pi\left[\frac{\mu}{r}\frac{\partial}{\partial r}(r\psi) + \xi\frac{\partial}{\partial z}\psi\right] = 2\pi\frac{\mu\psi}{r} - \frac{2\phi_r}{\sigma_t}\left(\mu^2 - \xi^2\right) + 2\phi_r(\mu r + \xi z) \tag{5.4}$$

$$2\pi\left[-\frac{1}{r}\frac{\partial}{\partial\omega}(\eta\psi)\right] = -2\pi\frac{\mu\psi}{r} - \frac{2\phi_r}{\sigma_t}\left(\eta^2\right) \tag{5.5}$$

$$2\pi \times \sigma_t\psi = \sigma_t\left[\phi_0 + \left(r^2 + z^2\right)\phi_r\right] - 2\phi_r(\mu r + \xi z) \tag{5.6}$$

$$2\pi \times \frac{1}{2\pi}\left(\sigma_s\phi + Q\right) = \sigma_t\left[\phi_0 + \left(r^2 + z^2\right)\phi_r\right] - \frac{2\phi_r}{\sigma_t} \tag{5.7}$$

Note how the equation is satisfied because all terms of same color cancel. Some parts of the spatial derivative cancel with some parts of the angle derivative term, this means that the spatial and angular discretization methods have to work conjointly to achieve the same kind of cancellation. This is not easy to achieve. In the following sections we demonstrate the results for each method discussed in this research. The plots provided are produced by an iterative code written in Python given the following parameters,

$$N_i \equiv \text{number of cells in the } r \text{ axis}$$

$$N_j \equiv \text{number of cells in the } z \text{ axis}$$

$$N_p \equiv \text{number of polar angles}$$

$$N_a \equiv \text{number of azimuthal angles}$$

$$R \equiv \text{radius of the sphere}$$

$$\sigma_t \equiv \text{total cross section}$$

$$\sigma_s \equiv \text{scattering cross section}$$

$$\phi_0 \text{ and } \phi_r \equiv \text{manufactured solution arbitrary constants}$$

The numbering of corners in a cell is shown in Fig.(5.1).

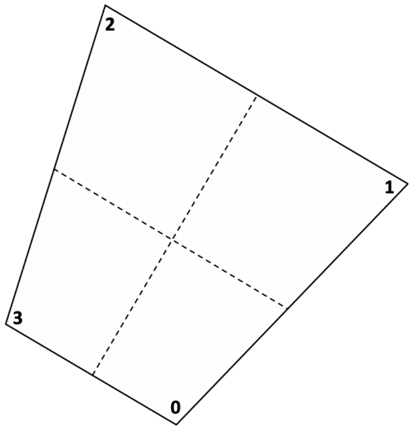

Figure 5.1: Numbering of corners in a cell.

5.2 Asymmetry of G-PWLD

The G-PWLD method is the state-of-art method that we began with in this research. It has all of the desired properties except that its preservation of spherical symmetry is not as good as desired. In this section, we show the asymmetry of the G-PWLD method by computing the relative deviation for each ringside,

$$RD_{i,(0,3)} = \left| \frac{\sqrt{\sigma^2_{i,(0,3)}}}{\bar{\phi}_{i,(0,3)}} \right| \tag{5.8}$$

$$RD_{i,(1,2)} = \left| \frac{\sqrt{\sigma^2_{i,(1,2)}}}{\bar{\phi}_{i,(1,2)}} \right| \tag{5.9}$$

where

$$\bar{\phi}_{i,(0,3)} = \frac{1}{2N_j} \sum_j^{N_j} \phi_{i,j,0} + \phi_{i,j,3} \tag{5.10}$$

$$\bar{\phi}_{i,(1,2)} = \frac{1}{2N_j} \sum_j^{N_j} \phi_{i,j,1} + \phi_{i,j,2} \tag{5.11}$$

$$\sigma^2_{i,(0,3)} = \frac{1}{2N_j} \sum_j^{N_j} \left(\phi_{i,j,0} - \bar{\phi}_{i,(0,3)}\right)^2 + \left(\phi_{i,j,3} - \bar{\phi}_{i,(0,3)}\right)^2 \tag{5.12}$$

$$\sigma^2_{i,(1,2)} = \frac{1}{2N_j} \sum_j^{N_j} \left(\phi_{i,j,1} - \bar{\phi}_{i,(1,2)}\right)^2 + \left(\phi_{i,j,2} - \bar{\phi}_{i,(1,2)}\right)^2 \tag{5.13}$$

To explain what a ringside is, we take for example the 2-cell geometry, the number of cells in r direction (N_i) is 1 and number of wedges along z axis (N_j) is 2. So there are two ringsides, one for corners 0 and 3, and one for corners 1 and 2 along the wedges. As shown in Fig (5.2)(a), the plot shows that the relative deviation is less on the outer ringside (corners 1,2). We also plot the scalar

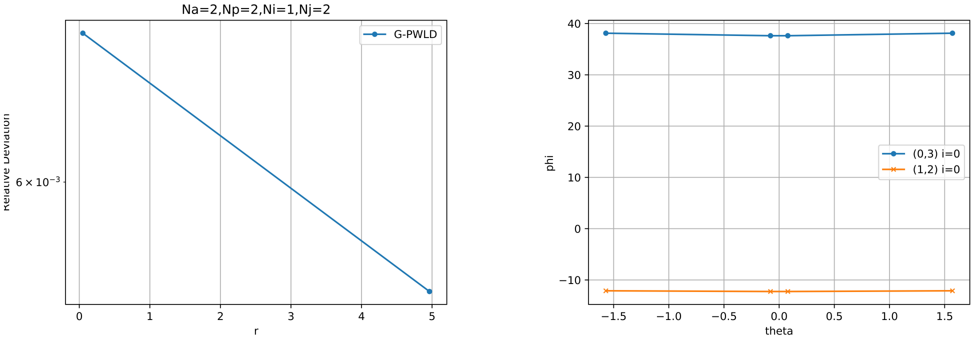

(a) Relative Deviation

(b) ϕ vs θ

Figure 5.2: Pure absorber 2-cell geometry with 2 azimuthal and polar angles.

flux for each ringside as a function of the angle $\theta \in \left(-\frac{\pi}{2}, \frac{\pi}{2}\right)$ in Fig (5.2)(b), where θ equals to $-\frac{\pi}{2}$ on the negative z axis, zero on the r axis, and $\frac{\pi}{2}$ on the positive z axis as previously illustrated in Fig(1.1). We plot each ring by itself in to be able to demonstrate the difference of values along θ, this is shown in Fig(5.3). Furthermore, we explore a slightly refined mesh with more azimuthal and polar angles, where $N_i = N_j = 4$ and $N_p = N_a = 16$. Figures (5.5) and (5.6) show that the scalar flux on the ringsides, are highest on z axis by about 0.1 from the lowest value. In Fig (5.4), the relative deviation is between 10^{-3} and 10^{-2}. Even though this is not terribly asymmetrical, we seek to improve the symmetry even more.

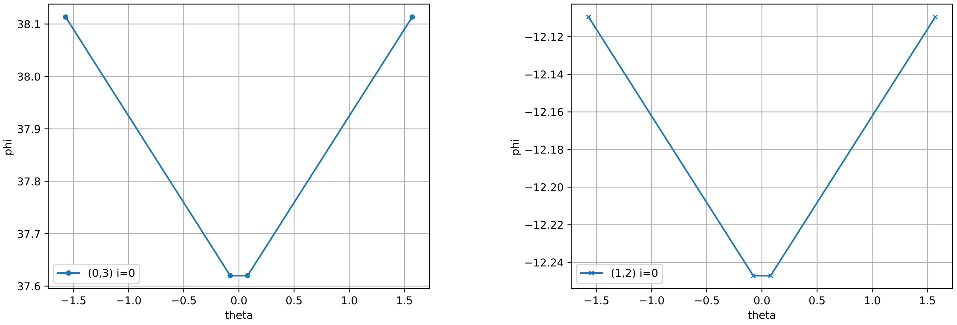

(a) (0,3) ring

(b) (1,2) ring

Figure 5.3: Scalar flux along wedges for a pure absorber 2-cell geometry with 2 azimuthal and polar angles.

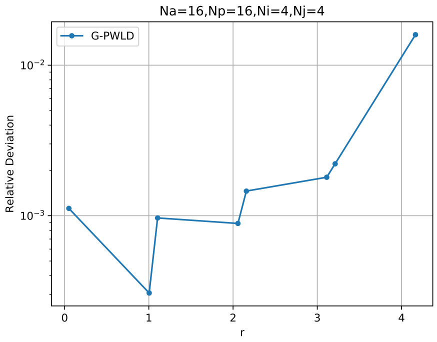

Figure 5.4: ϕ vs θ for ringsides 1 and 2

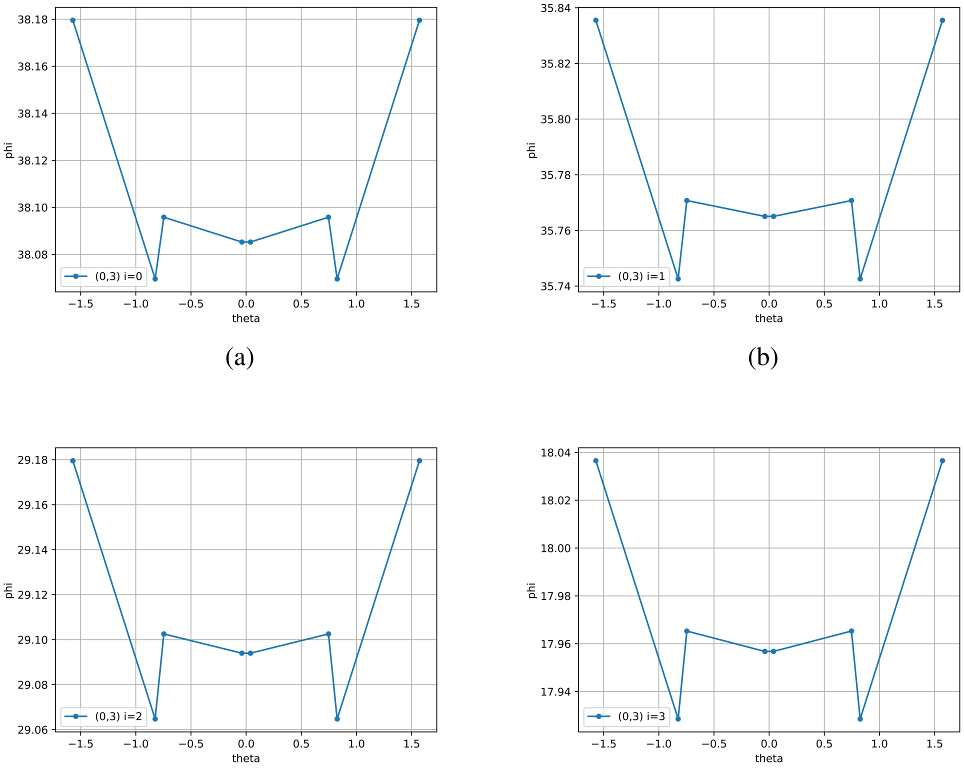

(a) (b)

(c) (d)

Figure 5.5: ϕ vs θ for ringsides 0 and 3

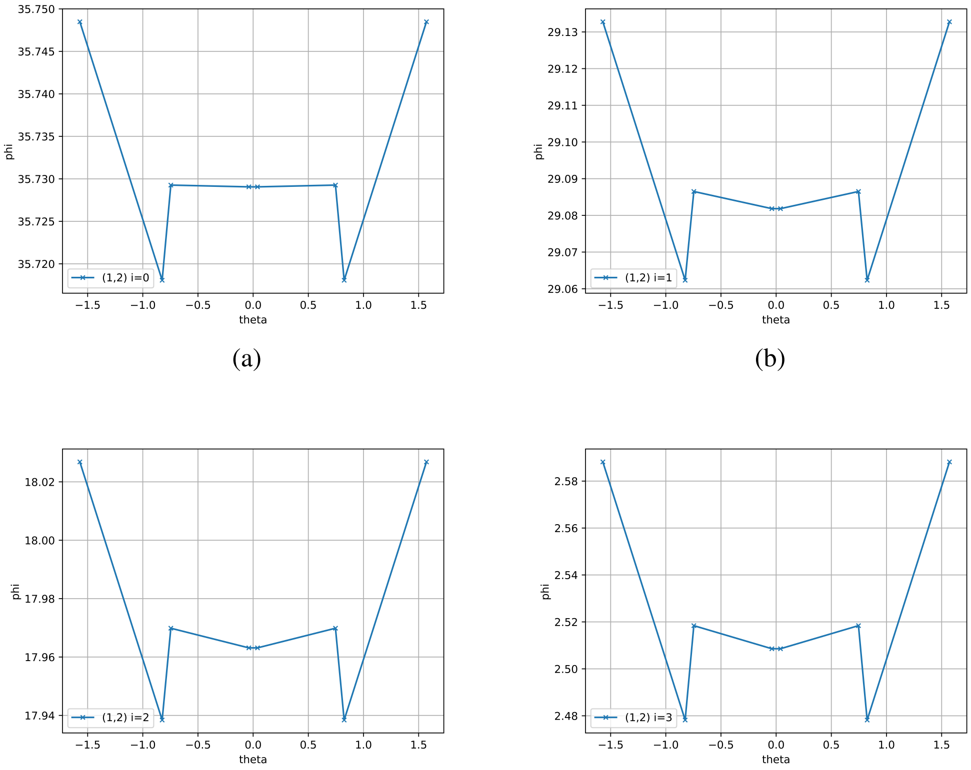

(a) (b)

(c) (d)

Figure 5.6: ϕ vs θ for ringsides 1 and 2

5.3 Modification to SCB-MB

In this section, we discuss a modification we made to the approximation for $\langle\psi\rangle_{c\pm1/2}^{p,q+1/4}$ in Eq.(4.22), which can also be written as follows

$$\left\langle \tilde{\psi} \right\rangle_{c\pm\frac{1}{2}}^{p,q+\frac{1}{4}} \approx \psi_c^{p,q+\frac{1}{2}} + \frac{1}{2}\Delta\psi^{p,q} \tag{5.14}$$

We used this approximation to avoid solving an 8x8 system of equations. As shown in Fig.(5.7), with only 2 cells and 2 azimuthal and polar quadrature points, the relative deviation is 10^{-4}, which is better than G-PWLD. However, when we refine the mesh by increasing the number of wedges $N_j = 160$, we start to see extreme oscillations at the cells closest to the center, as shown in Fig.(5.8). Figure(5.9) shows how the relative deviation jumps to 10^3 at the center. It appears that the reason for such behavior is that when the wedges get small enough, at certain directions some

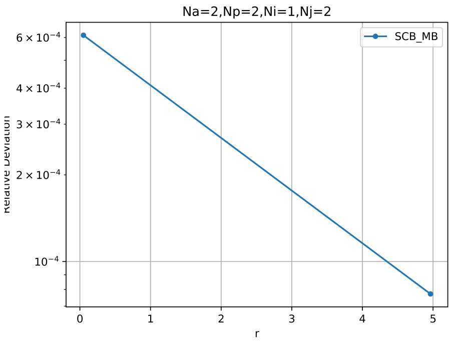

Figure 5.7: Relative deviation of a two cell problem for SCB-MB

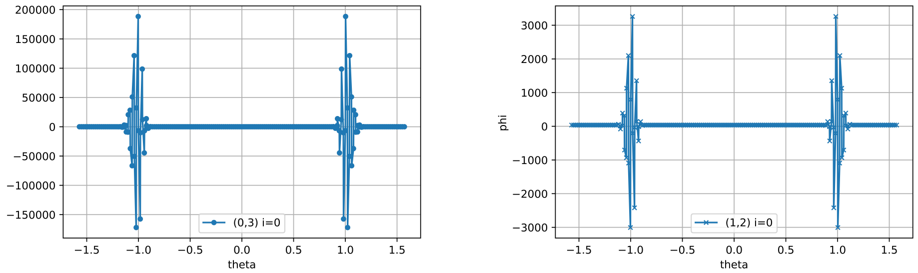

(a) (b)

Figure 5.8: SCB-MB scalar flux for inner most cells (upper) $N_p = N_a = 4$

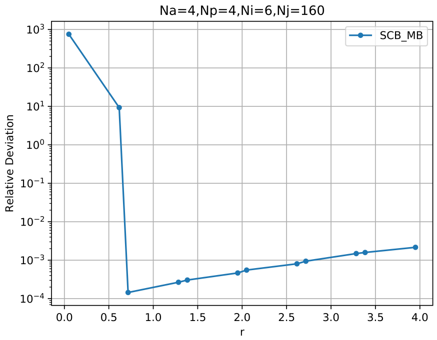

Figure 5.9: Relative deviation of SCB-MB problem $N_j = 160$

wedges become re-entrant. This means that the p, q direction cross some surfaces from one way and $p, q + \frac{1}{4}$ direction cross surfaces from the opposite way. In order to find the term causing the oscillations, we omitted the $\Delta\psi^{p,q}$ term in Eq.(5.14),

$$\left\langle \tilde{\psi} \right\rangle_{c\pm\frac{1}{2}}^{p,q+\frac{1}{4}} \approx \psi_c^{p,q+\frac{1}{2}} \tag{5.15}$$

And as illustrated in Fig. (5.10), with this approximation the scalar fluxes at the inner cells do not oscillate. This is confirming that the $\Delta\psi$ term is causing the oscillations, but we have not confirmed if this is a coding error or a method problem. Note that removing the $\Delta\psi$ term is not good approximation and it will not achieve the desired symmetry. As shown in Fig. (5.11), the relative deviation for the problem increases on the outer rings that already have good symmetry when we use the approximation with $\Delta\psi$ term. We use this approximation only to show results

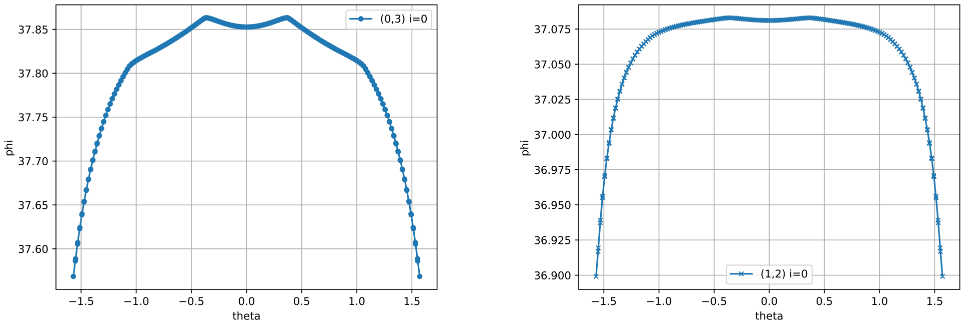

(a) (b)

Figure 5.10: SCB-MB scalar flux for inner most cells without $\Delta\psi$, $N_p = N_a = 4$

without oscillations.

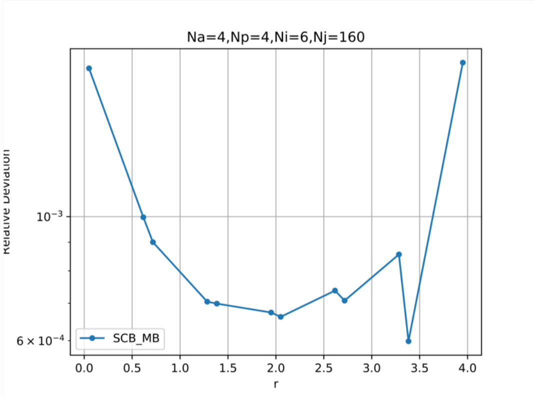

Figure 5.11: Relative deviation of SCB-MB problem without $\Delta\psi$, $N_j = 160$

5.4 Void Problem

In addition to the manufactured solution we are using, we ran some test problems using a different spherically symmetric boundary condition, incident on a source-free void:

$$\psi_{inc2}(r, z, \mu, \xi) = \frac{1}{2\pi}\left[C_0 + C_1(r\mu + z\xi)^2\right] \tag{5.16}$$

where $C_0 = 6$ and $C_1 = 2$, to show the behavior of solution when $\sigma_t = Q = 0$. Figure(5.12), shows the relative deviation of the four methods in the void problem. Note that for all the results demonstrated in this section the SCB-MB is using the approximation shown in Eq. (5.15). This is not an accurate approximation, but we apply it to our test problems to verify that it eliminates the oscillations that arose for certain problems when Eq. (5.14) was used.

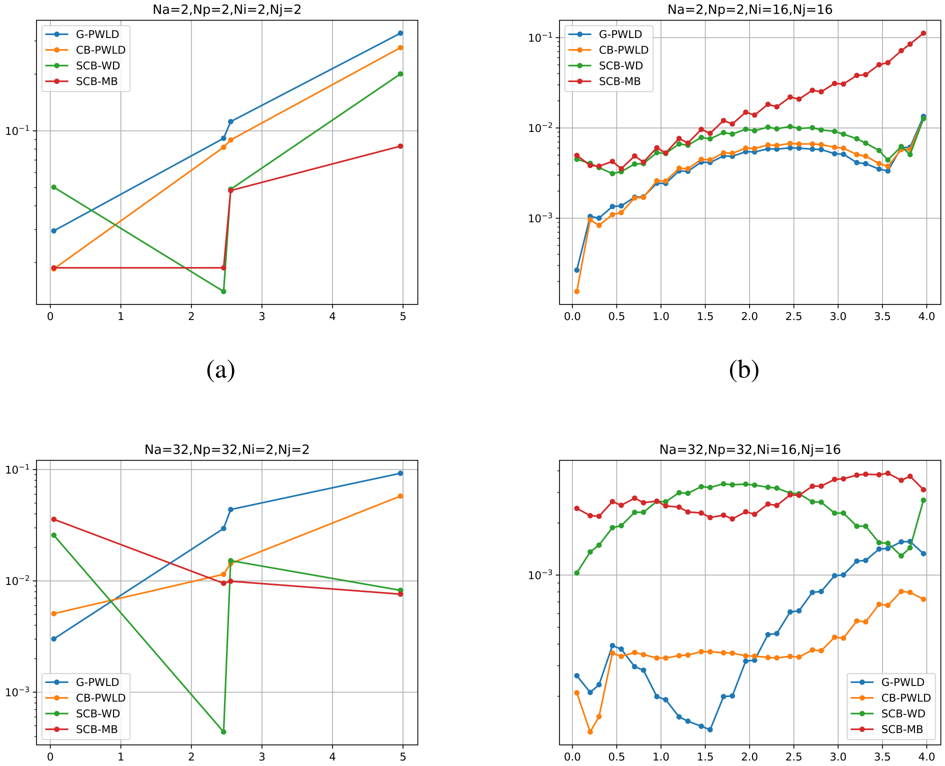

(a) (b)

(c) (d)

Figure 5.12: Relative deviation of the void problem for different N_i, N_j, N_a, and N_p.

5.5 Spherical Problem without Scattering

In this section, we will present the symmetry behavior of four methods, G-PWLD, CB-PWLD, SCB-WD, and SCB-MB. We use different mesh dimensions and different numbers of azimuthal and polar quadrature points. We plot the relative deviation, and scalar flux along wedges for some ringsides. First, we start with G-PWLD. In Fig(5.13), the scalar flux in highest on the z axis at the outer cell ((c) and (d)) and at the center point of the grid (a). Increasing N_a and N_p to 16, makes the solution flatter except at the z axis and center point, as shown in Fig(5.14). In Fig (5.15), the

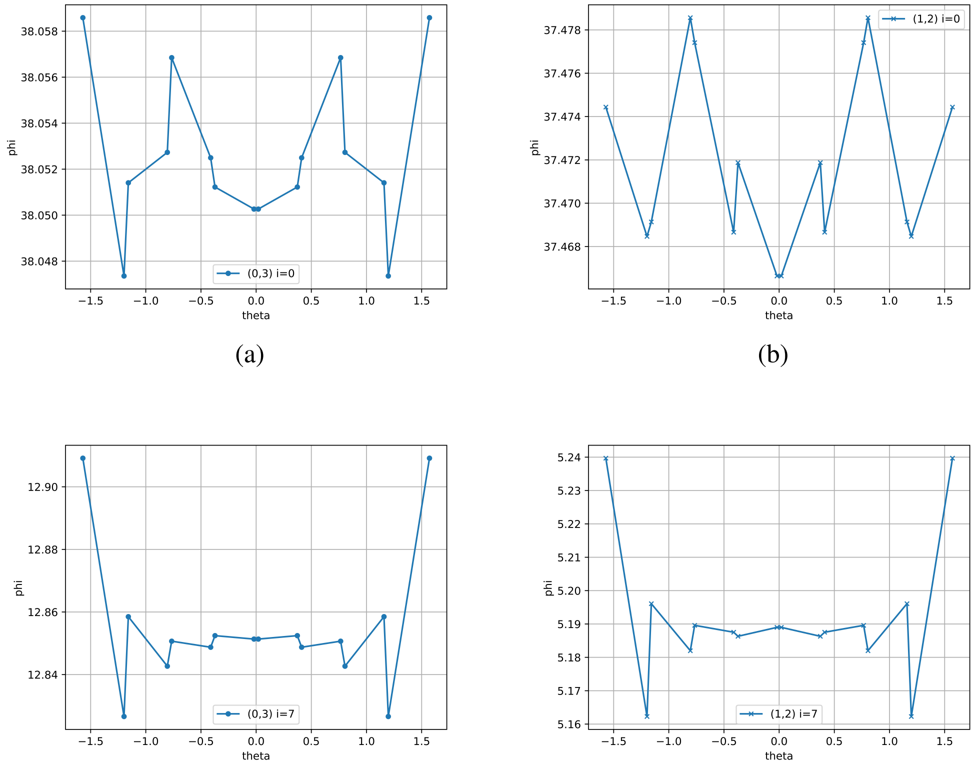

(a) (b)

(c) (d)

Figure 5.13: G-PWLD scalar flux for inner most cells (upper) and outer cells (lower) $N_p = N_a = 2$

plot for the scalar fluxes in all the rings for $N_p = N_a = 16$ shows how flat the flux values really are. In Fig (5.16), the scalar flux is shown as a function of θ for (0,3) and (1,2) ringsides for the inner most cells and cells on the boundary. With 8 cells in the r and z direction, and only 2 azimuthal and polar quadrature points, the difference in values along one ring is about 0.007. If

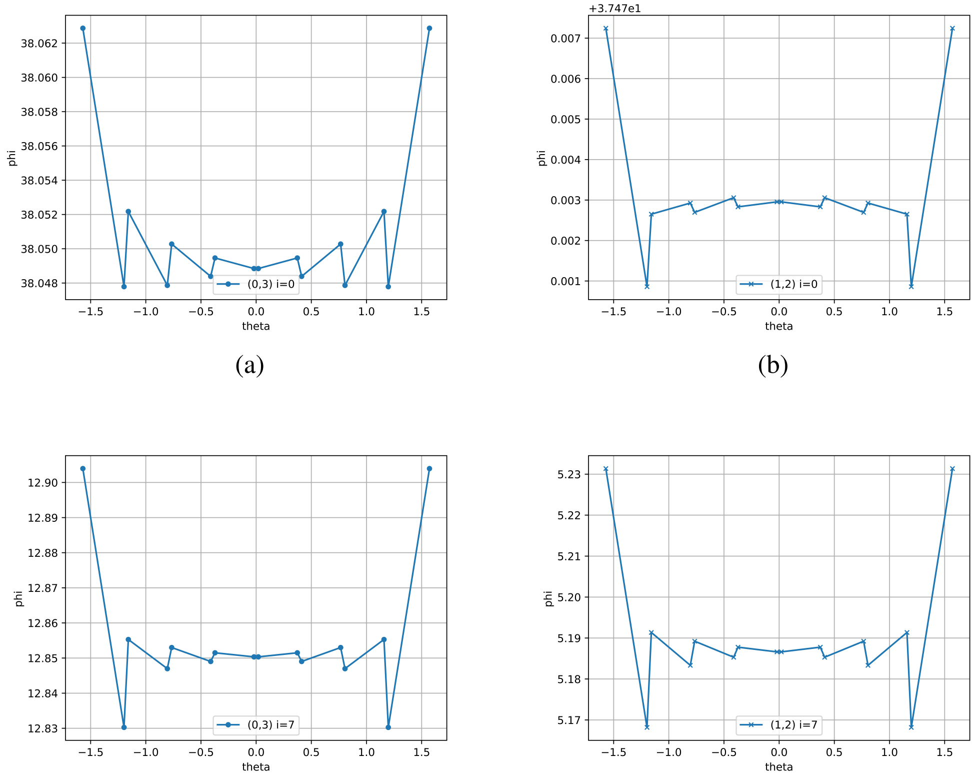

(a) (b)

(c) (d)

Figure 5.14: G-PWLD scalar flux for inner most cells (upper) and outer cells (lower) $N_p = N_a = 16$

we increase N_a and N_p to 16, we get a flatter behavior except for values on the z axis as illustrated in Fig.(5.17). And the plot for the scalar fluxes in all the rings for $N_p = N_a = 16$ is illustrated in Fig (5.18). Similarly, we plot the same results for SCB-WD in Fig (5.19) and (5.20), and for SCB-MB shown in Fig(5.22) and (5.23). Note that the deviation along the ring for the scalar flux in SCB-MB drops to 10^{-3} for the outer cell when using $N_a = N_p = 16$. We also plot the scalar flux for all rings in Fig (5.21) for SCB-WD. The plots in Fig.(5.24) illustrate the relative deviation as a function of the distance from the center of the geometry. The upper plots are for a 4 cell geometry with 4 (a) and with 64 (b) direction quadrature points. For the lower plots we use 32 cells with 4 (c) and with 64 (d) direction quadrature points. Note that the CB-PWLD shows better symmetry in all cases than the G-PWLD. We also plot relative deviation in Fig (5.25)) for CB-PWLD and SCB-WD for $N_i = N_j = 8$ increasing N_a and N_p from 8(a) to 64(b) to show the difference in

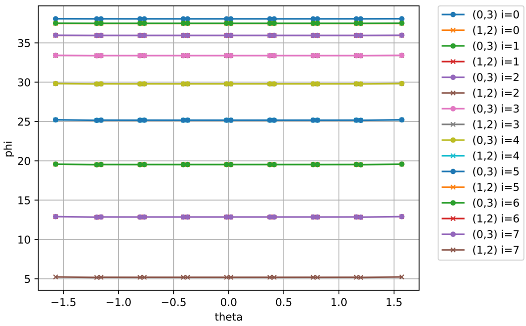

Figure 5.15: G-PWLD scalar flux for all rings $N_p = N_a = 16$

symmetry focusing on just these two methods. Furthermore, we plot the relative deviation for the other boundary condition ψ_{inc2} setting the source term to a constant in Fig. (5.26). Note how the symmetry of G-PWLD is worse than all other methods when $N_i = N_j = 2$, and how SCB-MB is not improving symmetry which is expected because of the crude approximation we are using. Additionally, we calculate the L_2-norm of scalar flux integrated over the volume of the geometry ($\bar{\phi}$),

$$||e||_{L_2} = ||\bar{\phi}_{sol} - \bar{\phi}_{ref}||_{L_2}/||\bar{\phi}_{ref}||_{L_2} \tag{5.17}$$

where $\bar{\phi}_{ref}$ is the scalar flux of the manufactured solution. In Fig.(5.27), we compare the error for each method when refining the mesh for different number of azimuthal and polar quadrature points. As illustrated, the error is not affected by the number of directions for the methods using the weighted diamond difference treatment. But, for the SCB-MB method as we refine the mesh we notice the error decreases when we use more azimuthal and polar quadrature points.

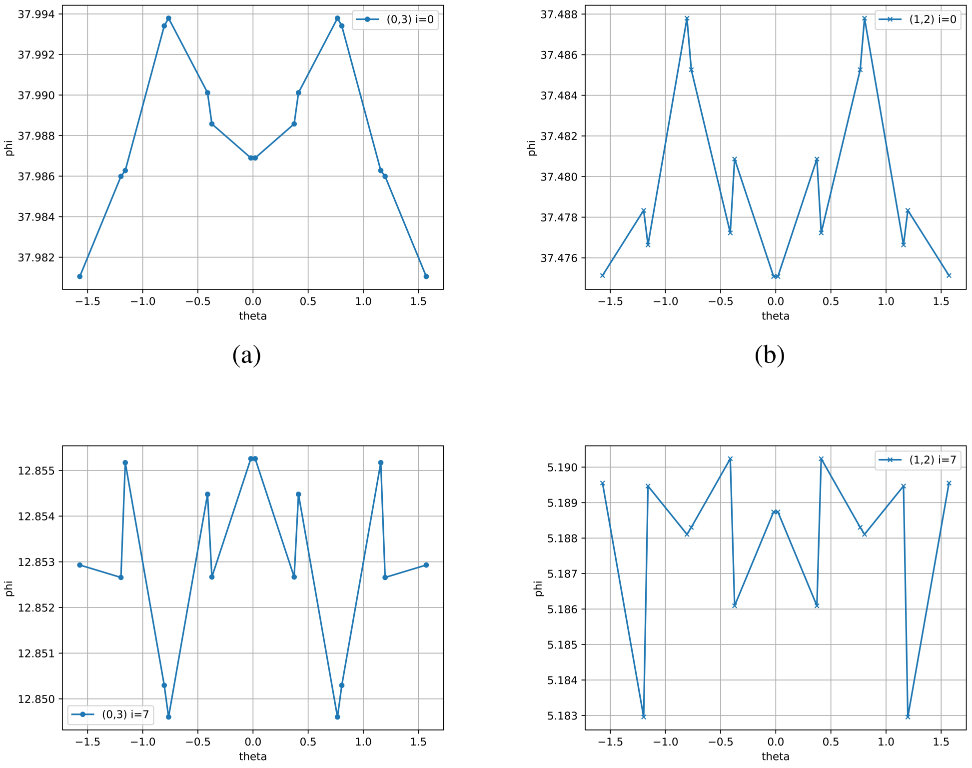

(a) (b)

(c) (d)

Figure 5.16: CB-PWLD scalar flux for inner most cells (upper) and outer cells (lower) $N_p = N_a = 2$

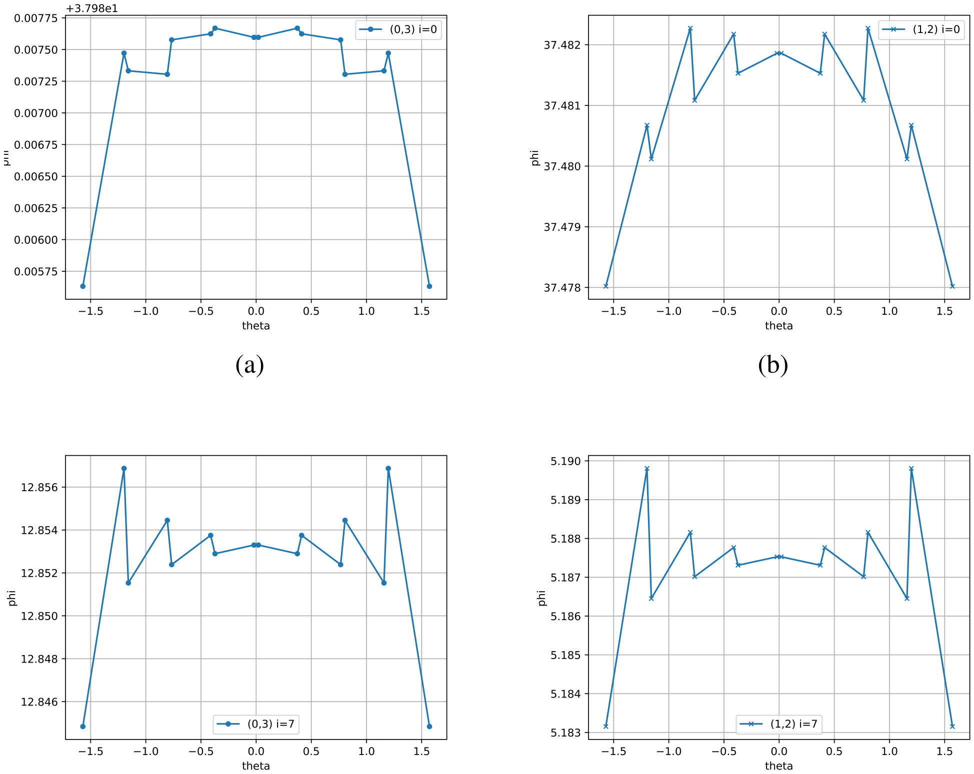

(a) (b)

(c) (d)

Figure 5.17: CB-PWLD scalar flux for inner most cells (upper) and outer cells (lower) $N_p = N_a = 16$

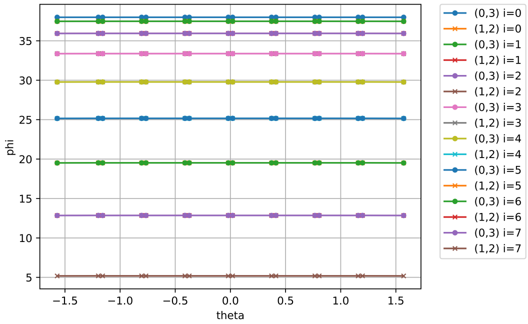

Figure 5.18: CB-PWLD scalar flux for all rings $N_p = N_a = 16$

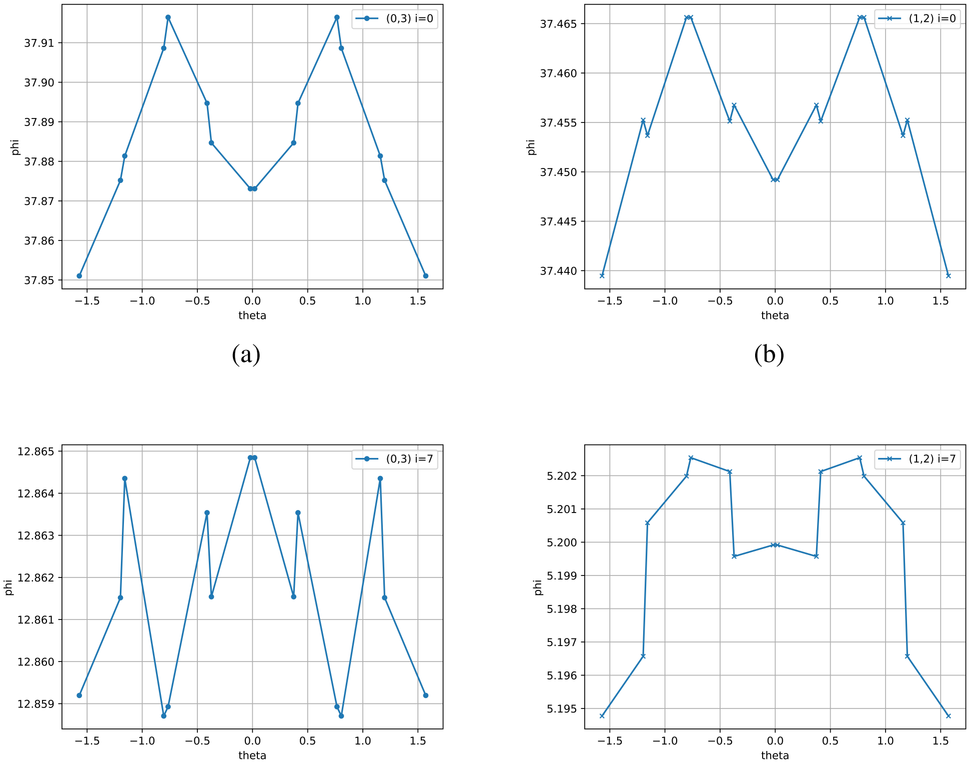

(a) (b)

(c) (d)

Figure 5.19: SCB-WD scalar flux for inner most cells (upper) and outer cells (lower) $N_p = N_a = 2$

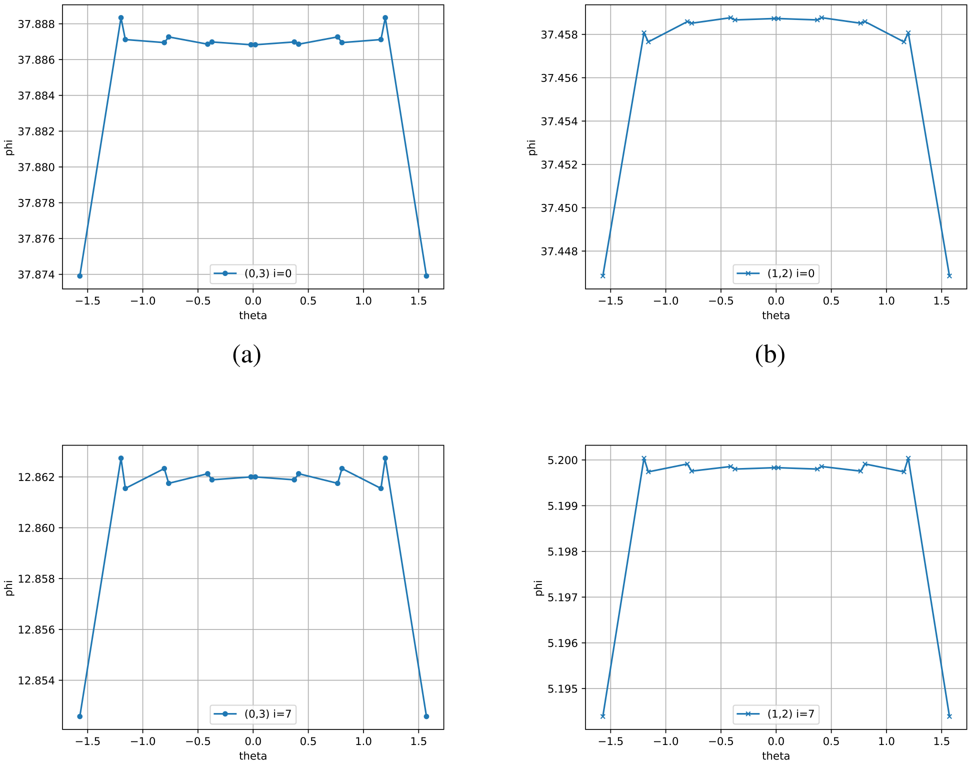

(a) (b)

(c) (d)

Figure 5.20: SCB-WD scalar flux for inner most cells (upper) and outer cells (lower) $N_p = N_a = 16$

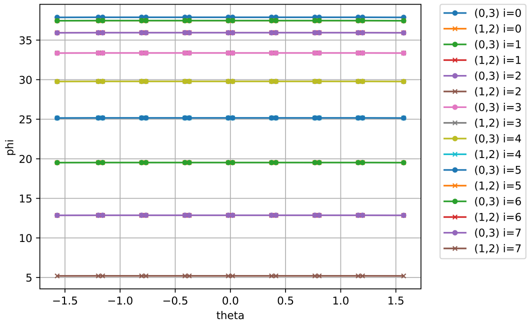

Figure 5.21: SCB-WD scalar flux for all rings $N_p = N_a = 16$

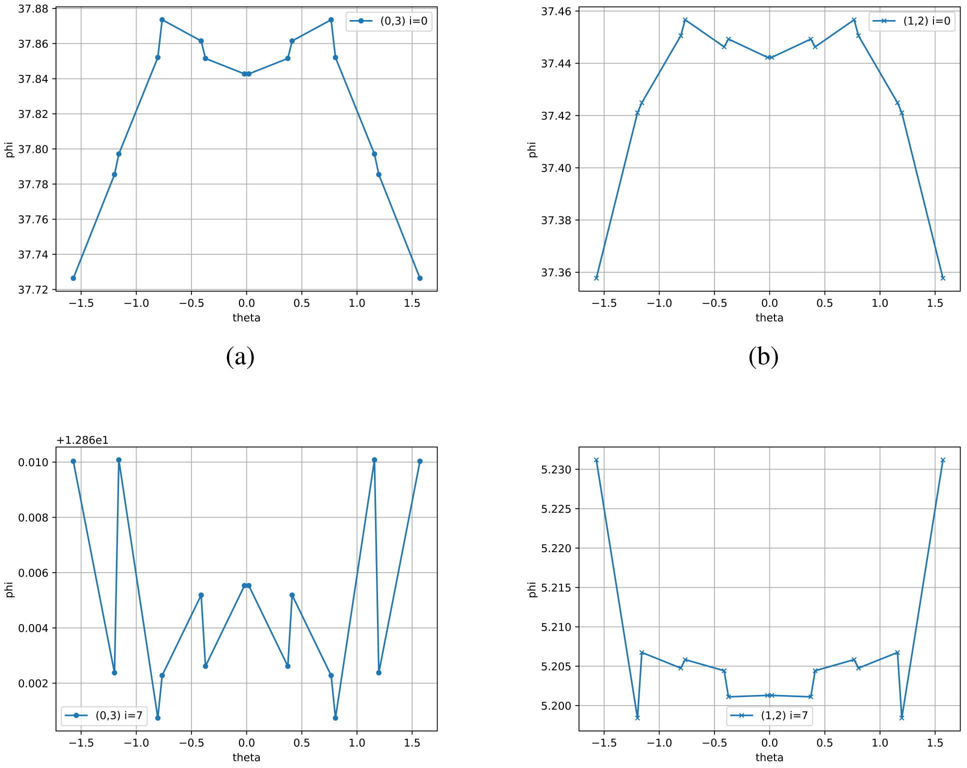

(a) (b)

(c) (d)

Figure 5.22: SCB-MB scalar flux for inner most cells (upper) and outer cells (lower) $N_p = N_a = 2$

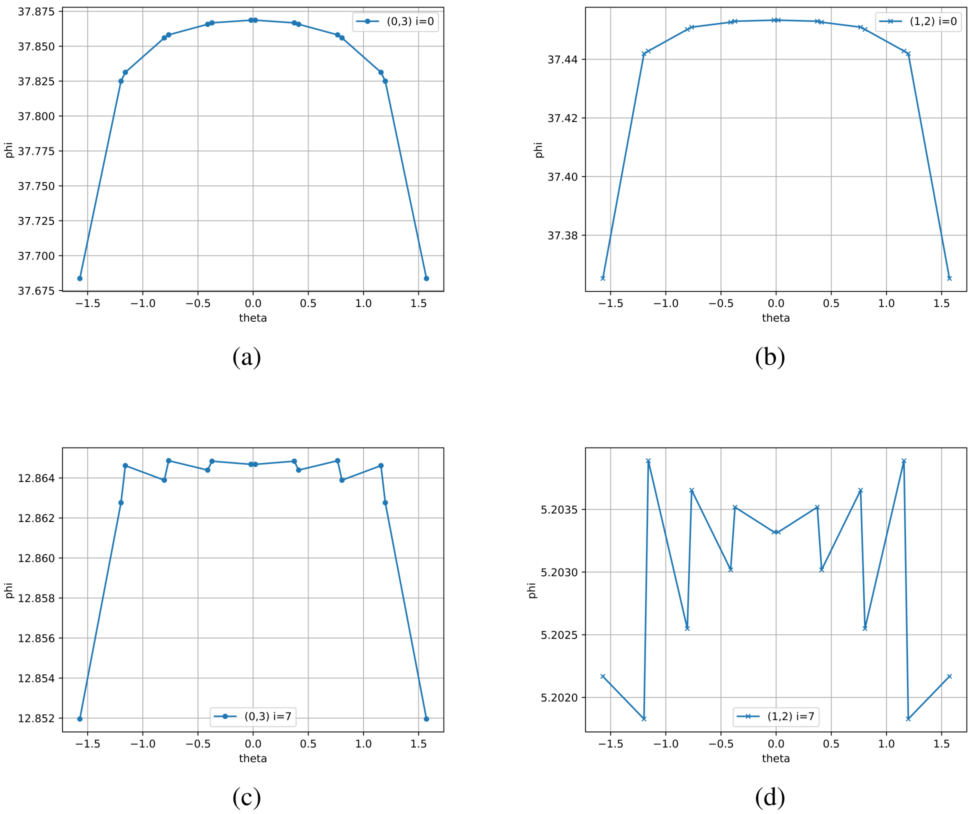

(a) (b)

(c) (d)

Figure 5.23: SCB-MB scalar flux for inner most cells (upper) and outer cells (lower) $N_p = N_a = 16$

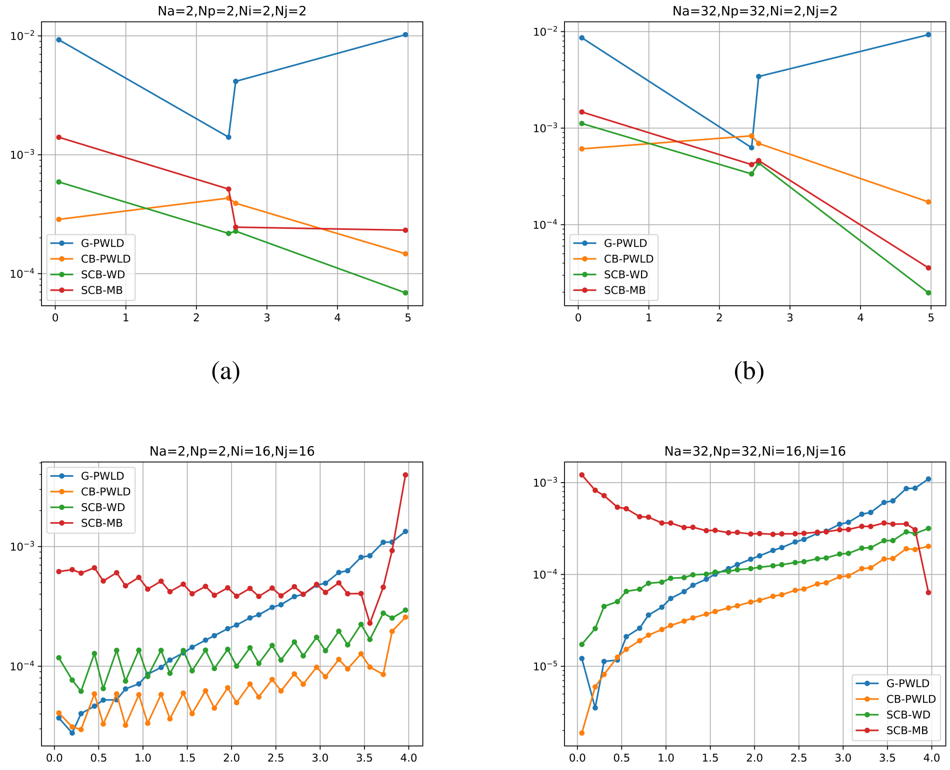

(a) (b)

(c) (d)

Figure 5.24: Relative deviation of the computed solution for ringsides as a function of distance from center.

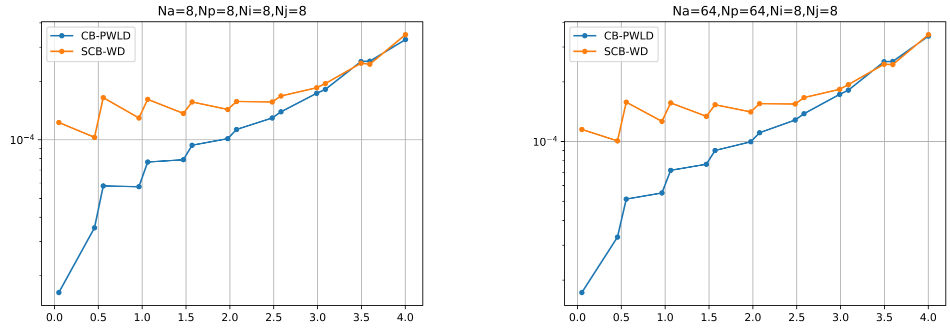

(a) (b)

Figure 5.25: Relative deviation of the computed solution for ringsides as a function of distance from center for CB-PWLD and SCB-WD.

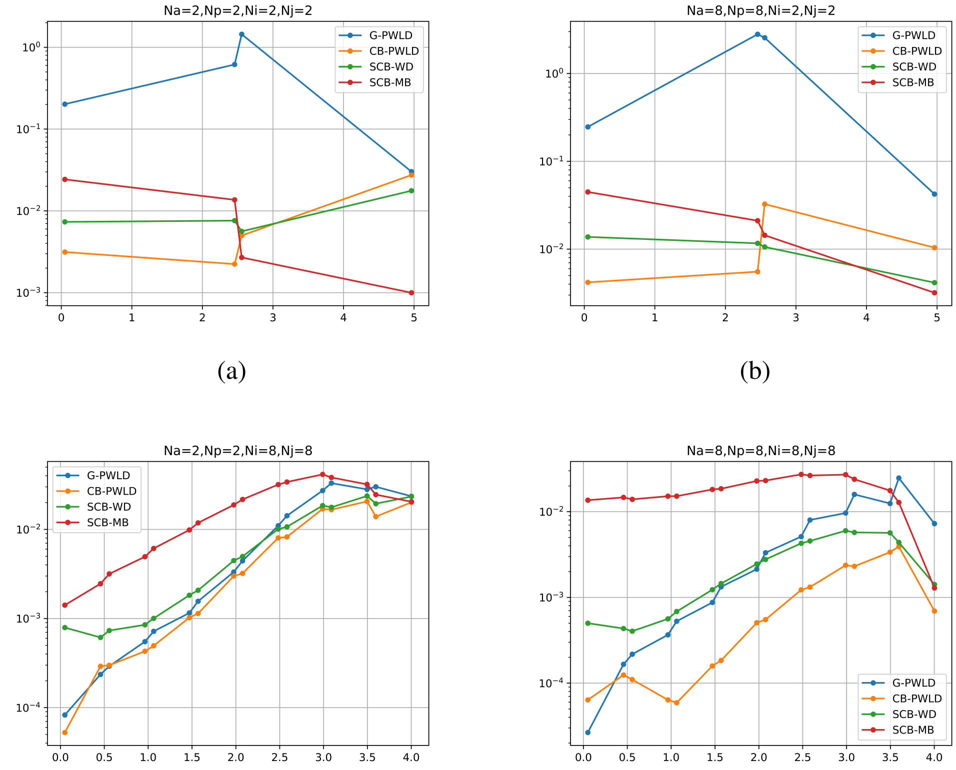

(a) (b)

(c) (d)

Figure 5.26: Relative deviation for ringsides as a function of distance from center using ψ_{inc2}.

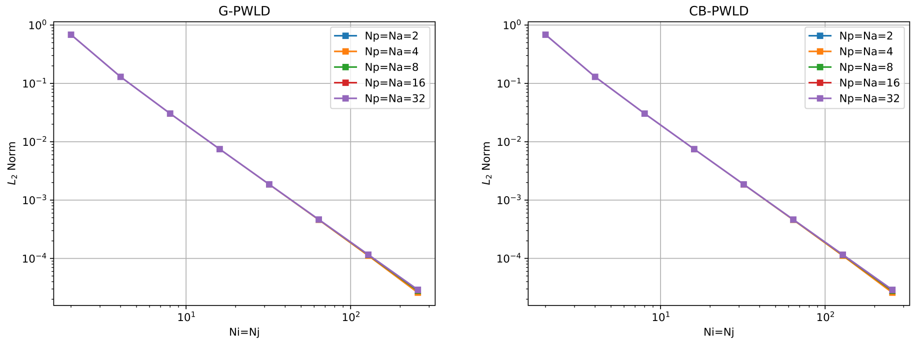

(a) G-PWLD-WD (b) CB-PWLD-WD

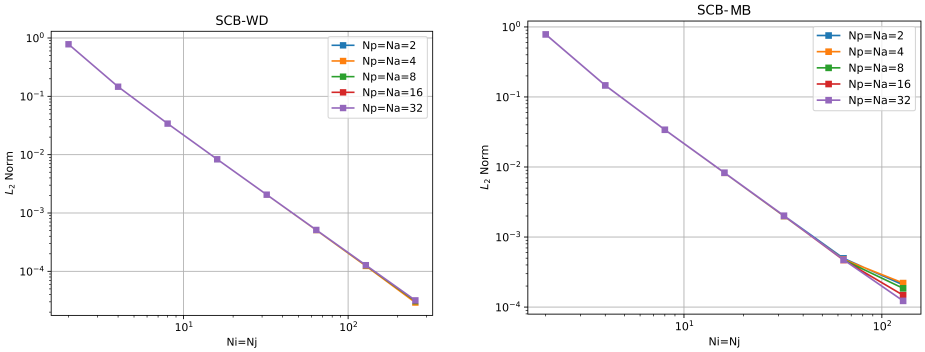

(c) SCB-WD (d) SCB-MB

Figure 5.27: L_2 norm of computed solution with respect to manufactured solution.

5.6 Spherical Problem with Scattering

In this section we explore the effect of adding scattering to the behavior of the computed solution. We plot the L_2 norm in Fig(5.28), we observe that the G-PWLD and CB-PWLD have the smallest error when refining the mesh. Also, SCB-MB method has better accuracy than SCB-WD if we use enough polar and azimuthal directions. Figure(5.29) shows the L_2 norm for the methods with $\sigma_s = 0.95\sigma_t$. Note in Fig(5.29 (d), it is clear we need to use more azimuthal and polar quadrature points for SCB-MB to reduce the norm. The difference is not very clear between the two scattering ratios because the scattering source is not entirely converged at 0.95 scattering ratio since we use tolerance of 10^{-4}. The relative deviation plots in Fig(5.30), show that SCB-MB and SCB-WD have better behavior when using small number of cells but CB-PWLD is better for a more refined mesh. In Fig.(5.31), we provide the relative deviation for all methods when $\sigma_s = \sigma_t$ with tolerance of 10^{-6}. From Fig.(5.31)(a) and (b), note that using more azimuthal and

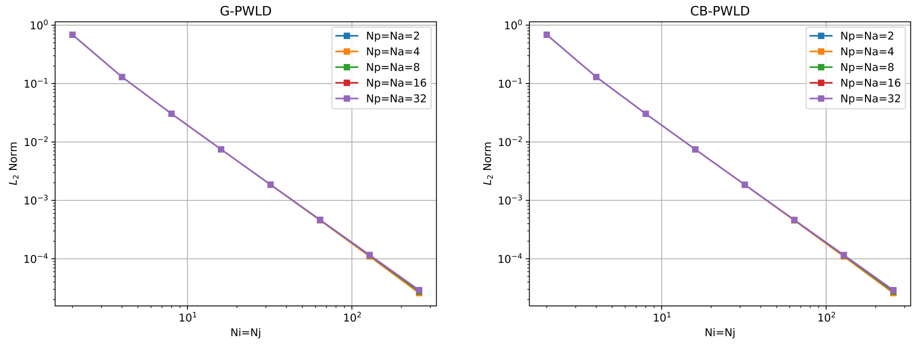

(a) G-PWLD-WD

(b) CB-PWLD-WD

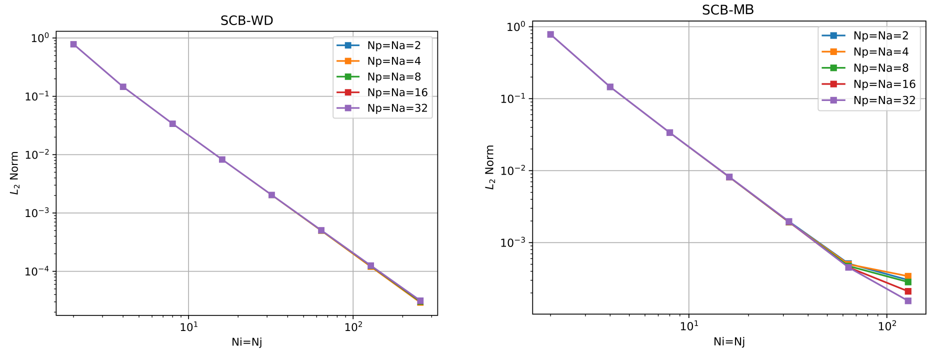

(c) SCB-WD

(d) SCB-MB

Figure 5.28: L_2 norm of computed solution with respect to manufactured solution with $\sigma_s = 0.5\sigma_t$.

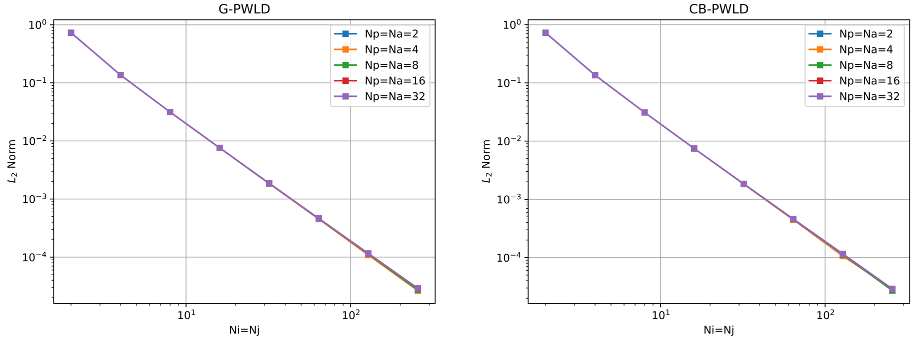

(a) G-PWLD-WD (b) CB-PWLD-WD

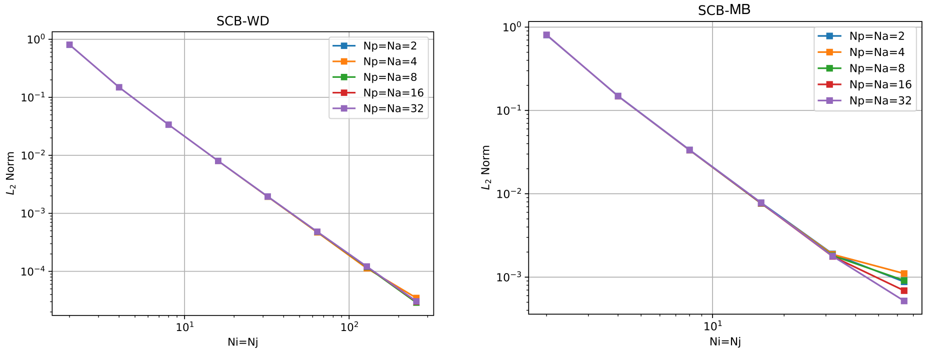

(c) SCB-WD (d) SCB-MB

Figure 5.29: L_2 norm of computed solution with respect to manufactured solution with $\sigma_s = 0.95\sigma_t$.

polar quadrature points in a 4 cell problem significantly decreases the relative deviation at the inner ring for CB-PWLD. In addition, we show the relative deviation of the four methods using the manufactured solution ψ_{inc2} of Eq.(5.16) setting the source term to a constant when scattering ratio is 1 in Fig (5.33) and when scattering ratio is 0.9 in Fig (5.32). Note that the G-PWLD and CB-PWLD behave the same when the mesh is refined but CB-PWLD is better for $N_i = N_j = 2$.

Finally, we show the scalar flux as a function of θ for the methods G-PWLD, CB-PWLD, SCB-WD and SCB-MB. Similar to the previous section, we show the ringsides of the inner most and boundary cells, but we only use the 64-cell mesh with $N_a = N_p = 16$. In Fig(5.36) the solution is changing by a factor of 10^{-1} in the ringsides of inner cells and 10^{-2} in the ringsides of outer cells, this deviation is caused by the fluxes on the z axis. We see in Fig(5.37) that the solution at the boundary cell is changing by a factor of 10^{-3} on (1,2) ringside.

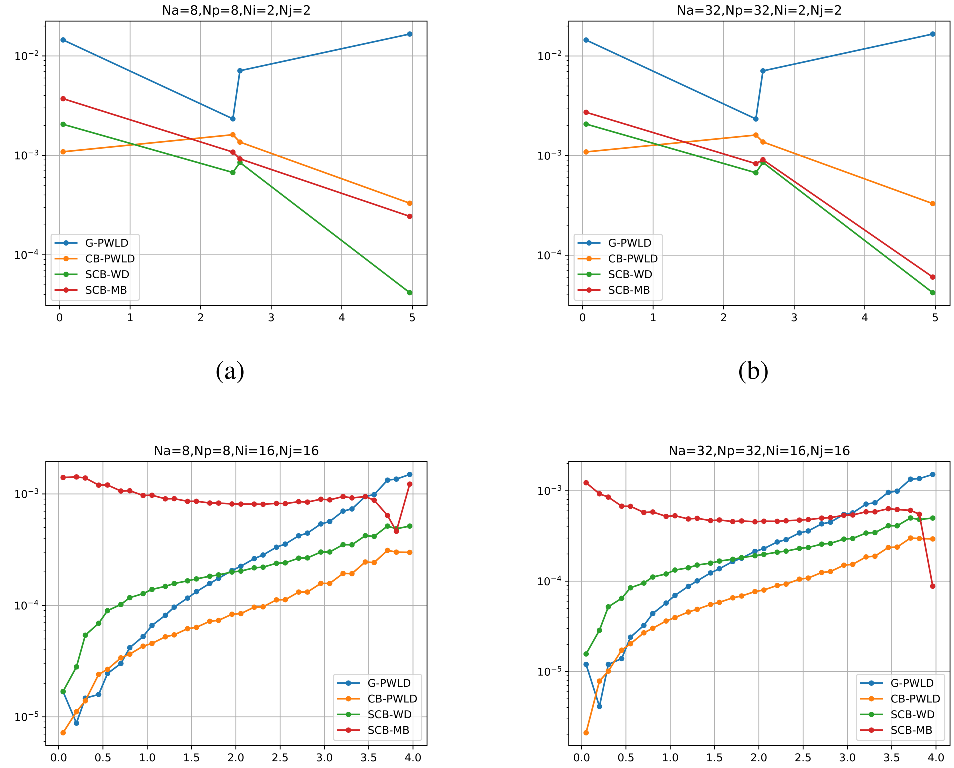

(a) (b) (c) (d)

Figure 5.30: Relative deviation of the methods with different N_a, N_p, N_i, and N_j when $\sigma_s = 0.5\sigma_t$.

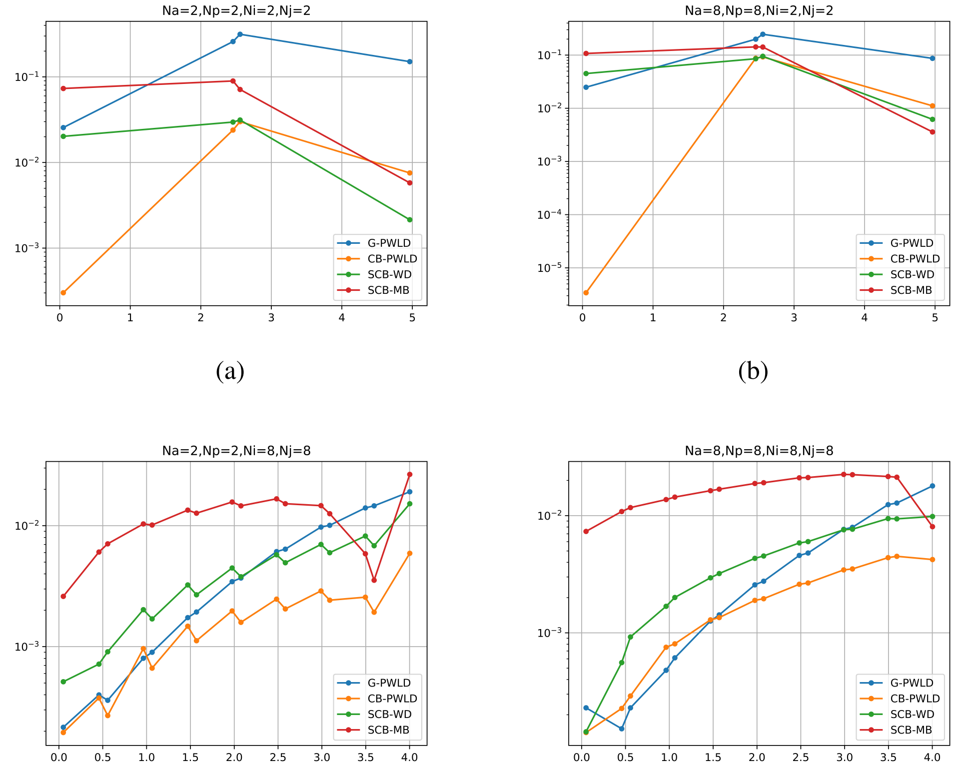

(a) (b)

(c) (d)

Figure 5.31: Relative deviation of the methods with different N_a, N_p, N_i, and N_j when $\sigma_s = \sigma_t$.

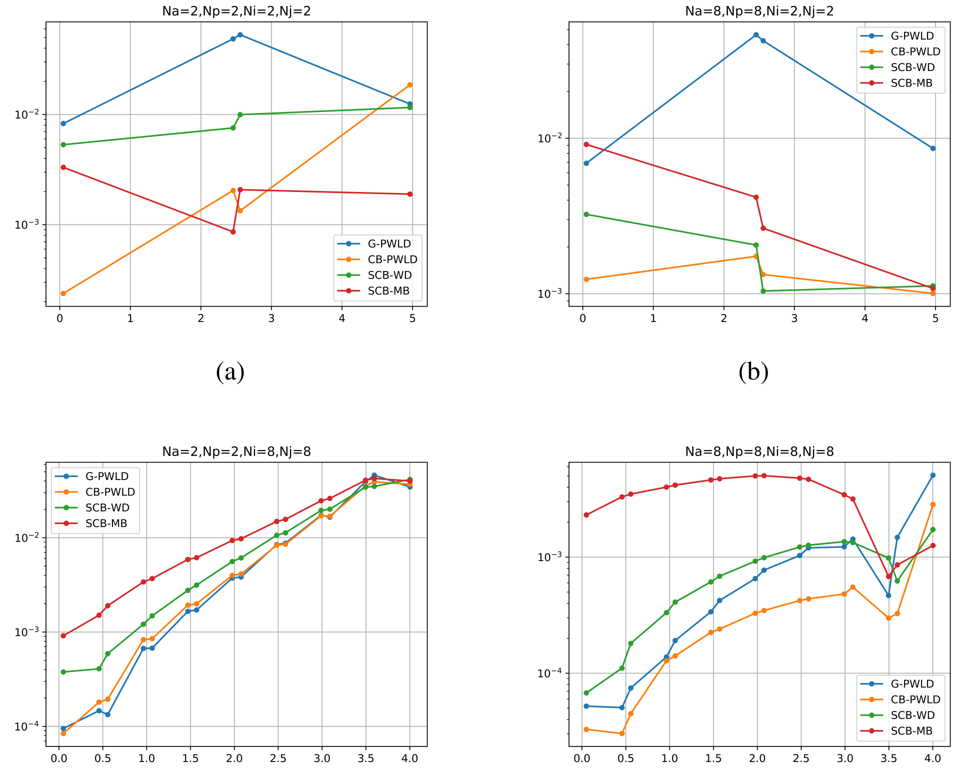

(a) (b)

(c) (d)

Figure 5.32: Relative deviation of the methods with different N_a, N_p, N_i, and N_j when $\sigma_s = 0.9\sigma_t$.

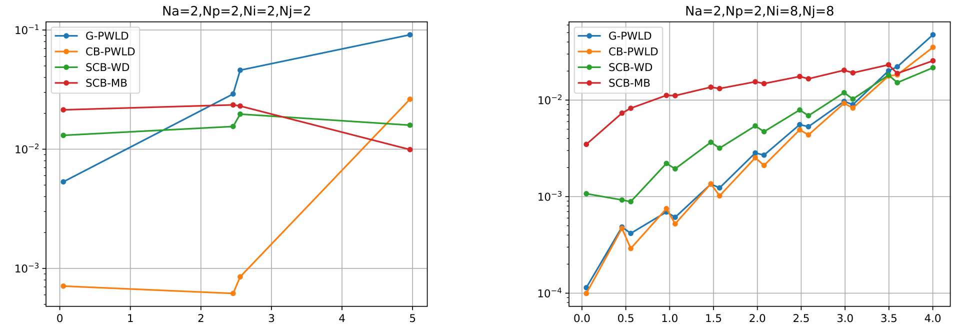

(a) (b)

Figure 5.33: Relative deviation of the methods with different N_a, N_p, N_i, and N_j when $\sigma_s = \sigma_t$.

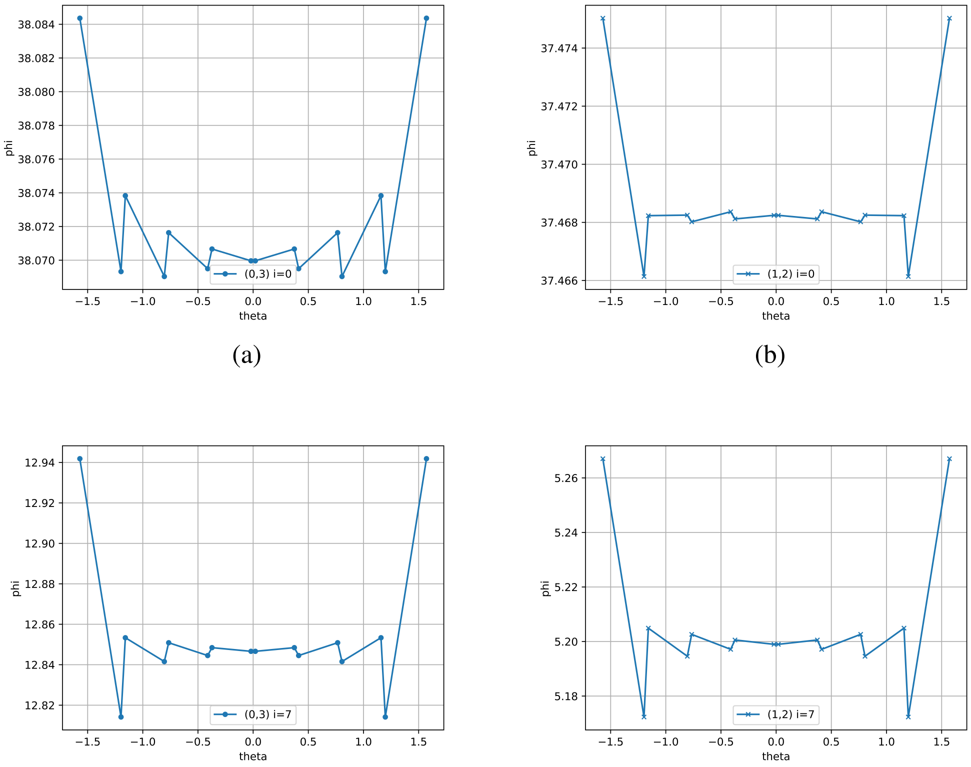

(a) (b)

(c) (d)

Figure 5.34: G-PWLD scalar flux for inner most cells (upper) and outer cells (lower) $N_p = N_a = 16$

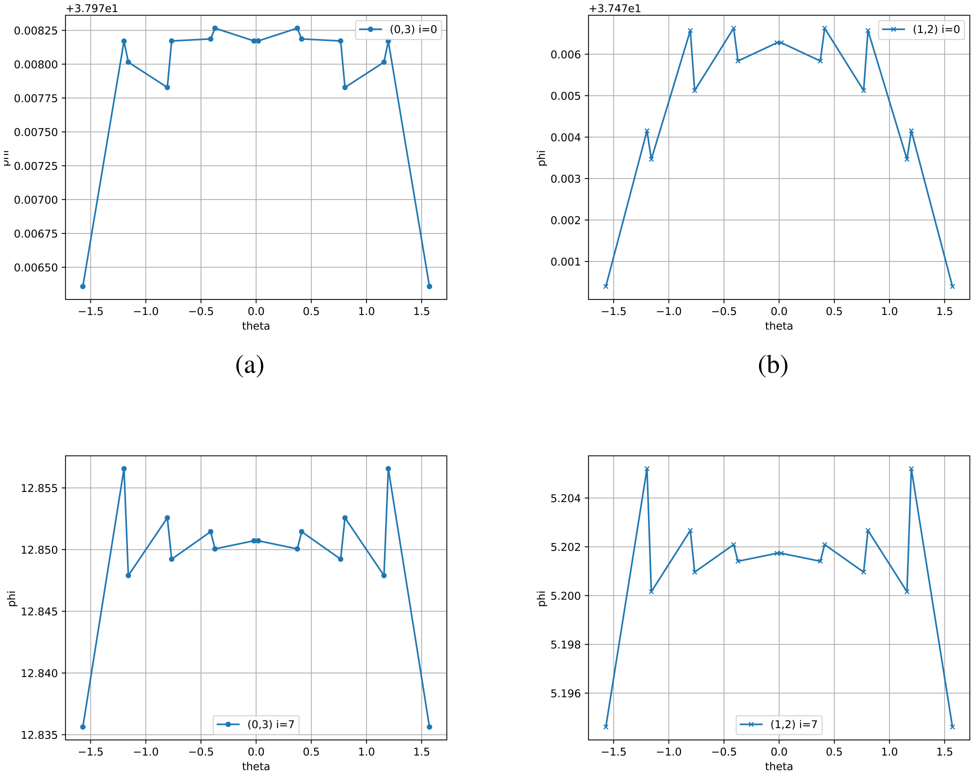

(a)

(b)

(c)

(d)

Figure 5.35: CB-PWLD scalar flux for inner most cells (upper) and outer cells (lower) $N_p = N_a = 16$

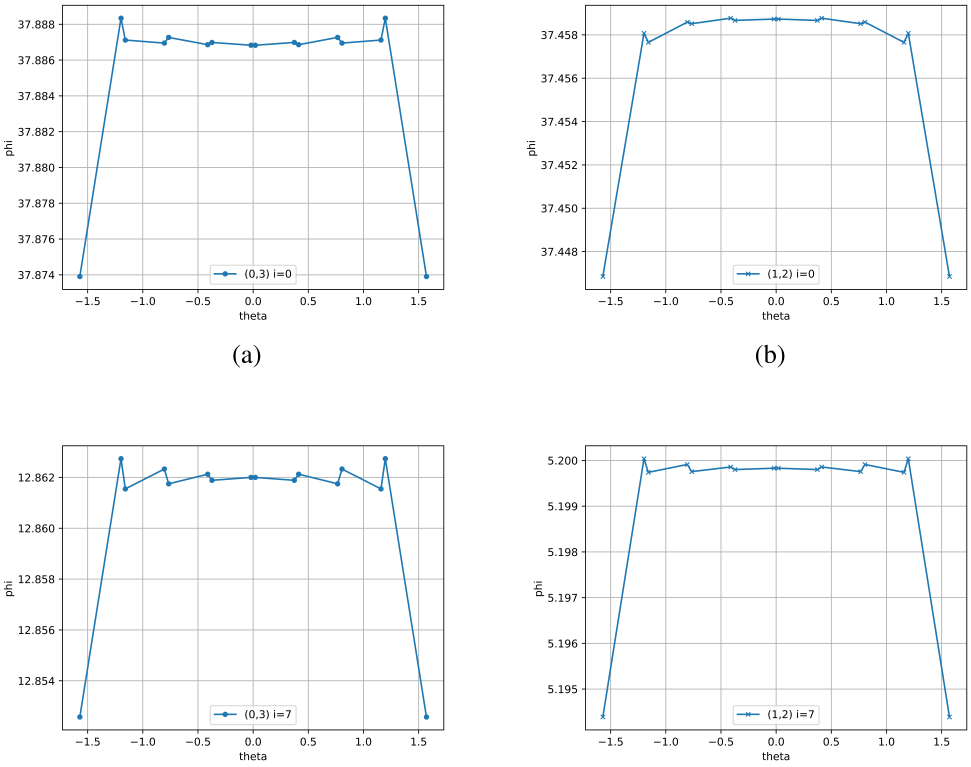

(a) (b)

(c) (d)

Figure 5.36: SCB-WD scalar flux for inner most cells (upper) and outer cells (lower) $N_p = N_a = 16$

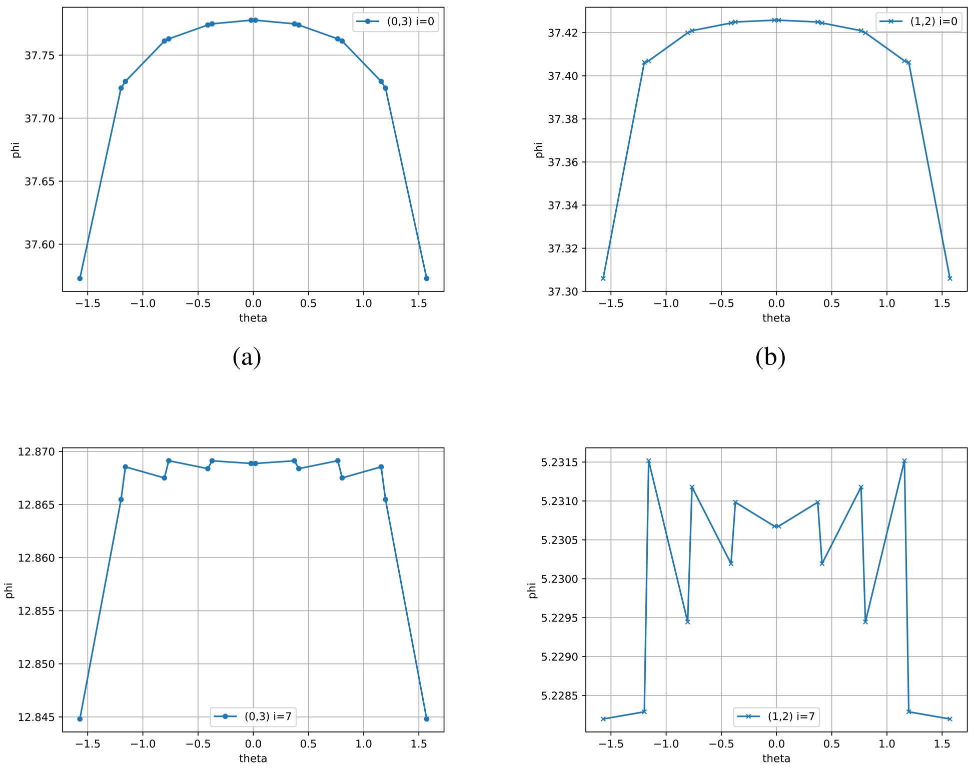

(a) (b)

(c) (d)

Figure 5.37: SCB-MB scalar flux for inner most cells (upper) and outer cells (lower) $N_p = N_a = 16$

5.7 Different Norms

We noticed that our norm plots look different from the plots generated by Dr. Ragusa and Dr. Caron. An example is shown in Fig.(5.38) where they illustrate the norm of discontinuous Galerkin. We speculate that the difference in plots is because we are using different grids, and because Ragusa and Caron obtain exact integrals of squared functions over each cell (the square of the exact solution or the square of the difference between the FEM and exact solution), whereas we have averaged the exact and discrete solutions over each cell before further operations, as defined below:

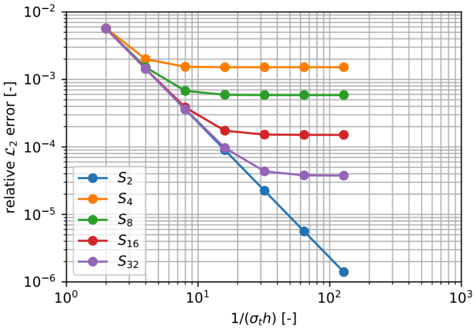

Figure 5.38: L_2 norm of discontinuous Galerkin.

$$||\bar{\phi}_{ref}||_{L_2} = \sqrt{\frac{1}{V_{sph}} \sum_{i}^{N_i} \sum_{j}^{N_j} V_{i,j} \left\langle \phi_{ref} \right\rangle_{i,j}^2} \tag{5.18}$$

$$||\bar{\phi}_{sol} - \bar{\phi}_{ref}||_{L_2} = \sqrt{\frac{1}{V_{sph}} \sum_{i}^{N_i} \sum_{j}^{N_j} V_{i,j} \left[\left\langle \phi_{sol} \right\rangle_{i,j} - \left\langle \phi_{ref} \right\rangle_{i,j} \right]^2} \tag{5.19}$$

$$\left\langle \phi \right\rangle_{i,j} = \frac{\sum_{c}^{corners} V_{i,j,c} \phi_{i,j,c}}{\sum_{c}^{corners} V_{i,j,c}} \tag{5.20}$$

These reasons are not confirmed yet.

5.8 Variation on Methods

In this section, we show various plots of some combinations we tried. For example, the first plot shown in Fig(5.39)(a), is the relative deviation of SCB-MB where we use the bin-wise averaging ratio. For reference, we show SCB-MB with ratio set to 1 (or when we use collocation) in Fig(5.39)(b). Note how the ratio value affects the symmetry on the ringsides. The bin-wise averaging ratio value produces better symmetry than collocation. Next, we show some results of using the Diamond-Like treatment for SCB. We show in Fig (5.40) and (5.41) the scalar flux as a function of θ for the inner and outer cell for the spherical problem, for $N_a = N_p = 2$ and $N_a = N_p = 16$, respectively. Also, we plot the relative deviation for the same problem when using bin-wise averaging and when using collocation as illustrated in Fig(5.42)(a) and (b) respectively.

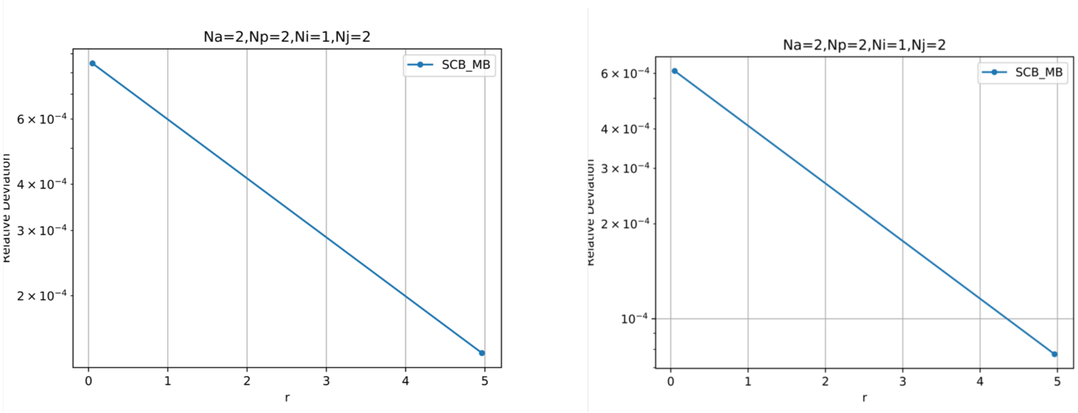

(a) (b)

Figure 5.39: Relative deviation of solution using different ratio values in SCB-MB mehtod.

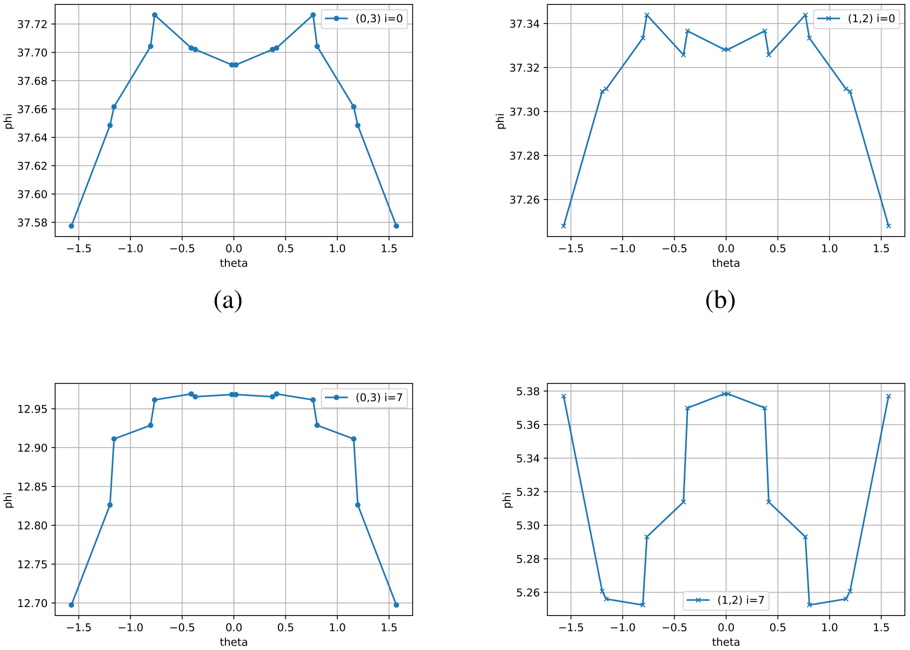

(a) (b)

(c) (d)

Figure 5.40: SCB-DL scalar flux for inner most cells (upper) and outer cells (lower) Np=Na=16

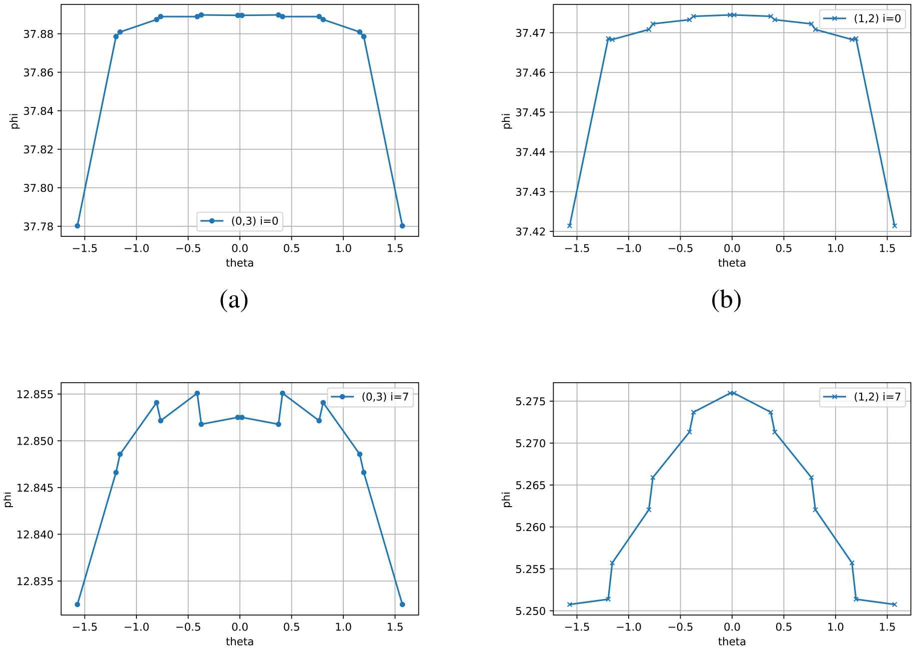

(a) (b)

(c) (d)

Figure 5.41: SCB-DL scalar flux for inner most cells (upper) and outer cells (lower) Np=Na=16

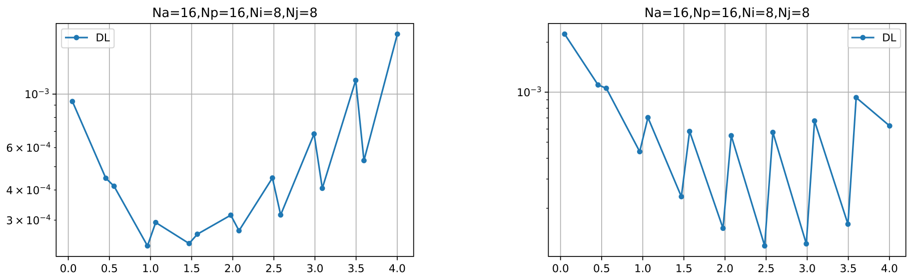

(a) (b)

Figure 5.42: Relative deviation of solution using different ratio values in SCB-DL mehtod.

6. CONCLUSIONS

6.1 Summary

In this research, we explored different spatial and angular discretization methods. We started with the ”Corner Balance Piecewise Linear Discontinuous” CB-PWLD method, we then introduced a generalized CB method where we use a family of averages of the angular fluxes in a cell. This method had better symmetry in the 2-cell problem but we realized that we can improve the symmetry and accuracy of the solution even further by treating the angle derivative term the same way we treat the spatial terms. So we started by a simple modification to the weighted diamond difference scheme where we derived an expression for $\psi_{p,q+\frac{1}{2}}$ using the weighted averages of the incident and exiting angular fluxes in a corner of the cell. We called this method the Diamond Difference-like method. Then, we introduced the MB method which is the main alternative to the WD treatment we consider. This method uses integration over angle bins.

We showed the numerical results of two different manufactured solutions using the methods discussed in the previous chapters. We conclude that CB-PWLD and SCB-WD achieve better symmetry G-PWLD. All methods achieve second order truncation error in the test problems. The SCB-MB method produce good symmetry small number of cells. We expect that SCB-MB can be improved once we confirm the source of oscillations. We also showed the difference between the use of collocation and bin-wise averaging, and we expect it can be further studied on different problems.

6.2 Future Work

As discussed in Section (5.3), we suspect that the difference in the L_2 norm plots can be a result of the use of different ways to calculate the L_2 norm or the different grids. We still need to confirm these speculations with further studies. We can explore the advantages and disadvantages collocation and bin-wise averaging. As illustrated in Section (5.5), bin-wise averaging gives better symmetry for SCB-MB method in a two cell problem. We need to investigate the symmetry and accuracy by trying more test problems using different number of rings and wedges in the spatial grid and different polar and azimuthal quadrature points.

The source of oscillations is confirmed to be the $\Delta\psi$ term of the approximation applied to $\langle\psi\rangle_{c\pm\frac{1}{2}}^{p,q+\frac{1}{4}}$. But, we still need to confirm whether it is caused by coding error or method problem. With the new angle derivative treatment, we have the option of using the approximation of $\psi_{c+1/2}^{p,q+1/2}$, or solve the eight by eight system of equations. We need to investigate whether solving the system without approximation will give us significantly better accuracy and symmetry of solution. We can also apply the MB treatment to CB integral equation and explore the effect of using the approximation or solving the 8x8 system.

REFERENCES

[1] W. F. M. E. E. Lewis, “Computational methods of neutron transport,” 1984.

[2] F. Chaland and G. Samba, “Discrete ordinates method for the transport equation preserving one-dimensional spherical symmetry in two-dimensional cylindrical geometry,” *Nuclear Science and Engineering*, vol. 182, no. 4, pp. 417–434, 2016.

[3] D. N. Woods and T. S. Palmer, “R-z geometry discrete ordinates radiation transport using higher-order finite element spatial discretizations on meshes with curved surfaces,” *Journal of Computational and Theoretical Transport*, vol. 48, no. 3, pp. 109–128, 2019.

[4] J. E. Morel and G. R. Montry, “Analysis and elimination of the discrete-ordinates flux dip,” *Transport Theory and Statistical Physics*, vol. 13, no. 5, pp. 615–633, 1984.

[5] M. L. Adams, “Discontinuous finite element transport solutions in thick diffusive problems,” *Nuclear Science and Engineering*, vol. 137, no. 3, pp. 298–333, 2001.

[6] T. Bailey, “The piecewise linear discontinuous finite element method applied to the rz and xyz transport equations,” *Doctoral Dissertation*, 2008.

[7] T. Palmer, “Curvilinear geometry transport discretizations in thick diffusive regions,” pp. 107–187, 1993.

[8] M. L. Adams, “Subcell balance methods for radiative transfer on arbitrary grids,” *Transport Theory and Statistical Physics*, vol. 26, no. 4-5, pp. 385–431, 1997.